TECHNISCHE UNIVERSITÄT WIEN

DIPLOMARBEIT

Photovoltaic Effect in van der Waals Heterostructures

von

Armin August Zechmeister, B.Sc.
0726851
Fleschgasse 22, 1130 Wien

Eingereicht an der
Fakultät für Physik
der **Technischen Universität Wien**

in Zusammenarbeit mit dem
Institut für Photonik

unter der Leitung von
Univ.Prof. Mag.rer.nat. Dr.rer.nat. Karl Unterrainer,
Ass.Prof. Dipl.-Ing. Dr.techn. Thomas Müller
und
Dipl.-Ing. Marco Mercurio Furchi‘

Wien, 11. Mai 2015 _____

Abstract

As the demand for alternative energy sources to fossil fuels has grown over the last years, photovoltaics have emerged to one of the most widespread technologies within renewable energy sources. Many different solar cell technologies have been developed over the last years, all aiming to improve efficiency in energy conversion while reducing material expenses and costs of production, which is a difficult task to fulfil. With the discovery of the natural existence of graphene and its stability under environmental conditions by A. Geim and K. Novoselov in 2004, the era of a new class of materials has been ushered in: the class of two-dimensional materials was born. These materials, crystals of only one atomic layer in thickness, exhibit unusual and exotic characteristics and have been explored by scientists over the last years, revealing a huge family of similar materials. A group of materials referred to as transition metal dichalcogenides (TMDC's) have earned special attention for their semiconducting properties. Among many electronic applications, the utilization of these materials as solar cells had been shown by building a 2-layer p-n heterojunction, though leaving several possibilities for modification and improvement.

In this work, the fabrication of triple-junction solar cells made of transition metal dichalcogenide thin films is presented. The principle of a simple p-n junction is altered by the introduction of a third layer that is expected to improve recombination losses at the heterojunction's interface.

Different fabrication methods were explored, and by combining the strengths of these methods a three layer heterostructure was built by stacking mono- or few-layer sheets on top of each other. The devices were fabricated onto a silicon substrate covered by an insulating oxide layer, making it possible to operate the devices under the influence of various gate fields and thereby tuning their electronic properties. A p-n type behavior could be found for negative gate voltages around -60 Volts, at which the devices were further investigated for their operation as a solar cell. The working principle of a three layer TMDC heterojunction as a solar cell was proven, power dependent measurements showed an increase in efficiency with rising optical power and a constant fill factor. Spatially resolved photocurrent measurements were performed to determine the distribution of current generation across the device.

Kurzfassung

Die stetig steigende Nachfrage nach alternativen Energiequellen zu fossilen Brennstoffen in den letzten Jahren hat Photovoltaik zu einer der weitverbreitetsten Technologien innerhalb der erneuerbaren Energieträgern gemacht. Viele unterschiedliche Solarzellen Technologien wurden über die letzten Jahre entwickelt, alle mit dem Ziel die Effizienz der Energieumwandlung zu steigern bei gleichzeitiger Reduktion der Material- und Produktionskosten, was sich durchaus als schwierige Aufgabe darstellt. Als 2004 von A. Geim und K. Novoselov das natürliche Vorkommen und die Stabilität von Graphen unter atmosphärischen Umgebungsbedingungen nachgewiesen wurde, bedeutete das gleichzeitig den Beginn einer neuen Ära von Materialien die sich rasant in der Welt der Materialwissenschaften verbreitete: Die der zweidimensionalen Materialien. Diese Materialien, Kristalle mit der Dicke von nur einer Atomlage, weisen ganz besondere und ungewöhnliche Eigenschaften vor, und es dauerte nicht lange bis eine ganze Menge verschiedener solcher Materialien bekannt wurde. Einer Gruppe davon, die der Übergangsmetallchalcogene, (engl. TMDC's), wurde wegen ihrer ausgezeichneten Halbleitereigenschaften und ihrer potentiellen Anwendung in der Mikroelektronik besondere Aufmerksamkeit zuteil. Neben diversen elektronischen Bauteilen wurde auch ihre Verwendung als Solarzelle gezeigt. Durch das vertikale Stapeln zweier Dünnschichten wurde ein p-n Übergang geschaffen, jedoch lässt dieses Prinzip noch Raum für Modifikation bzw. Verbesserungen.

In dieser Arbeit wird die erfolgreiche Herstellung und Charakterisierung einer Drei-Schicht-Solarzelle aus Übergangsmetallchalcogenen präsentiert. Das bisherige Prinzip des einfachen p-n Übergangs wurde um eine Schicht erweitert, die in erster Linie dazu dienen sollte Rekombinationsverluste am Übergang der zwei Materialien zu reduzieren.

Verschiedene Methoden zur Herstellung wurden getestet und zu teilweise neuen Methoden kombiniert, sodass die erfolgreiche Herstellung eines dreifach-Übergangs durch stapeln einzelner Schichten erzielt werden konnte. Durch das Aufbringen der Bauteile auf isolierendem Siliziumdioxid konnte von der Rückseite ein elektrisches Feld zur Modifizierung der elektronischen Eigenschaften angelegt werden. Diodenartiges Verhalten konnte bei Gate-Spannungen von etwa -60 Volt festgestellt werden, bei welcher die Bauteile weiter auf ihre Funktion als Solarzelle untersucht werden konnten. Das Funktionsprinzip der Bauteile als Solarzelle konnte nachgewiesen werden, leistungsabhängige Messungen zeigten einen Anstieg der Effizienz mit steigender optischer Leistung und einen konstant bleibenden Füllfaktor. Weiters wurden ortsaufgelöste Photostrommessungen durchgeführt um die Verteilung der Stromerzeugung auf den Zellen zu bestimmen.

Contents

1. Introduction

In the last recent years energy supply became a widely discussed topic, due to the steadily growing global energy demand with ongoing development of states to industrial standards. At the same time traditional energy sources, mostly based on fossil fuels and combustion technologies, are obviously limited, forcing mankind to creatively search for new technologies to retain wealth and living standards, which are in direct correlation to the availability of energy. The aftermath of excessive emission of waste gases produced by fossil fuels starts to show its consequences within growing air pollution and an enhanced greenhouse effect, leading to more frequent extreme weather events, the melting of glaciers and the rise of the sea level to name just a few.

Since the first oil crisis in the 1970s, many new technologies have emerged showing the possibility for alternatives in energy harvesting. Among those, photovoltaics are one of the most uprising candidates for private as well as commercial alternative energy supply. By the conversion of sunlight into electrical energy they provide the most direct way of energy conversion for the generation of electrical energy, without the need of intermediate steps like preconversion to heat, kinetic energy or magnetism. Also within photovoltaics, a lot of technologies have emerged, beside the classical silicon solar cells there are various kinds of technologies reaching from hybrid organic-inorganic Perovskite-type cells to highly efficient optical concentrator systems, all having advantages and disadvantages, with their limiting factor for widespread commercialization mostly lying in short-term cost effectiveness.

Lately, a completely new class of materials has emerged, initiated by the discovery of graphene by A. Geim and K. Novoselov in 2004 [1]. Graphene can be seen as a carbon crystal similar to graphite, but with the smallest possible thickness of only one atomic layer. In fact, bulk graphite turned out to actually consist of a large number of adjacent graphene layers. It is not only astonishing that a material of this thickness is stable under ambient conditions, but also its material properties differ strongly from a graphite crystal extending to all three

dimensions. Its unique mechanical and electronic properties gained great interest in the scientific community and lead to the construction of various electronic devices based on this material [2–4]. For electronic engineering graphene however entails a certain disadvantage: its lack of a band gap and therefore its limited application in semiconductor electronics. At this point scientists' attention was drawn to a similar class of materials: transition metal dichalcogenides (TMDC's). As graphene, they are stable in a two dimensional form due to very strong in-plane bonds and weak out-of-plane bonds in the crystal lattice. [5] Their chemical structure is described by the formula MX_2, where M represents an element of the group of transition metals and X a chalcogen atom. In principle almost every combination of these atoms is possible, therefore a large variety of transition metal dichalcogenides exists and opens a huge field of research. As some of these materials (especially group six TMDC's) are semiconductors with variable band gaps which depend on the number of layers and are tunable by electric fields, they are of great interest for next generation electronic and optoelectronic devices.

As one of their novel applications, a photoelectric effect has been shown and their possible usage as solar cells has been proven [6–8]. To utilize two-dimensional materials as solar cells opens up new perspectives for photovoltaics, as for instance their semi-transparency makes application on windows and facades thinkable. Their mechanical stability would allow their application on flexible substrates and the amount of material needed to cover large areas[1] is reduced to an ultimate minimum due to their monomolecular thickness, which could drastically enhance cost efficiency if this technology is being developed to a commercial level.

In previously reported solar cells constructed of TMDC layers, two mono- or fewlayer materials with different doping were brought into contact to form a p-n junction and operate similar to the principle of classical single junction solar cells. The collection of photo-generated charge carriers seemed to be limited mostly by the immediate recombination of those electron-hole pairs at the p-n interface.

[1] For better illustration it could be said that one gram of TMDC material could cover the surface of more than a football field.

The aim of this work was to build a TMDC heterojunction made of three different layers to enable better spatial separation of the generated charge carriers and therefore enhance quantum efficiency. Various fabrication methods were explored and are presented in chapter 3. The devices and their performance as solar cells were characterized, as presented in chapter 4. A conclusion and an outlook is finally given in chapter 5. Chapter 2 provides background information for solar cells and TMDC materials.

2. Background

2.1. Solar cells

2.1.1. History of photovoltaics

The first time electrical energy was generated by a direct conversion from light dates back to 1876, when William Adams and Richard Day constructed a “solar cell” from a piece of selenium with platinum electrodes. This was the first proof that it was possible to convert solar radiation energy directly into electrical energy by a solid state body [9]. It further led to the invention of the first photometers based on selenium. The improved understanding of light-matter interaction, in particular by Planck’s law and Einstein’s explanation of the photoelectrical effect, formed the basis of new technological progress in the following years. The invention of the Schottky-diode in 1938 was a further building block for photovoltaic technology, in 1948 the first concept for a metal-semiconductor solar cell was developed by Lehovec [10]. One year later, W. Shockley presented the first semiconductor-semiconductor p-n diode which should be the cornerstone for modern photovoltaics [11].

In 1954 Chapin et al. published a work where they showed a photovoltaic effect in a Silicon p-n junction for the first time, which is the actual working principle of the solar cells most commonly used today [12]. The theoretical prediction of a solar cell efficiency limit <50% by Shockley and Queisser in 1961 [13] and the difficult and expensive production process of silicon kept the utilization of this technology from going much beyond extraterrestrial applications [10].

Not before the world energy crisis in the 1970ies the need for energy sources alternative to fossil fuels started to grow and gave path to the application of photovoltaic technology for terrestrial use. The accidents in nuclear powerplants in Harrisburg 1979 and particularly in Chernobyl in 1986 emphasized the public demand for safe renewable energy sources, and the requirement of being economically competitive led to new materials and technologies in photovoltaics [14, 15].

2.1.2. Solar radiation

Stefan Boltzmann's law describes the emissive power (j) of a black body radiator in terms of its thermodynamic temperature

$$j = \sigma * T^4$$

where $\sigma = \frac{2\pi^2 k^4}{15c^2h^3} = 5{,}670373 * 10^{-8}\,[Wm^{-2}K^{-4}]$ is the Stefan-Boltzmann-constant. With a given temperature at the surface of the sun of 5778 K [16] the solar emissive power per square meter is $j_{sun} \cong 6{,}32 * 10^7\,[Wm^{-2}]$. The sun radiates its power isotropic to all directions, thus multiplication with the suns total surface yields the total emitted power:

$$J_{tot} = j_{sun} * 4 * {r_{sun}}^2 * \pi \cong 3{,}84 * 10^{26}[W]$$

with $r_{sun} = 6{,}95508 * 10^8[m]$. [16] At the distance of the earth, this power is distributed equally over an imaginary sphere with approximately the radius of the earth-sun distance $A_{sphere} = 4 * {r_{dist}}^2 * \pi$. Therefore one obtains the irradiance power per square meter reaching the outer atmosphere of earth by dividing the total emitted power by the surface of this imaginary sphere:

$$E_S = \frac{J_{tot}}{A_{sphere}} = \frac{3{,}84 * 10^{26}[W]}{2{,}81 * 10^{23}[m^2]} \cong 1366\,[Wm^{-2}]$$

considering $r_{dist} = 1{,}496 * 10^{11}[m]$ [16] as the mean distance between earth and sun. E_S, also referred to as the solar constant or AM0, is the power per square meter reaching earth outside the atmosphere. The exact amount of radiation reaching the earth's surface is reduced by reflection, absorption and scattering effects and is therefore dependent on the light's way through the atmosphere. For this reason the air mass coefficient AMx is defined, where x denotes the ratio of the absolute optical path length through the atmosphere relative to the shortest path, i.e. 90 degrees to the earth's surface, or

$$x = \frac{1}{\sin\gamma}$$

if γ is the elevation angle of the sun [10]. This shortest path through the atmosphere thus is referred to as AM1, the most important value for characterizing solar power generation is AM1.5 which equals an incident angle of 48.2° relative to the zenith and a global irradiation power of $1000\ [Wm^{-2}]$ [10] .

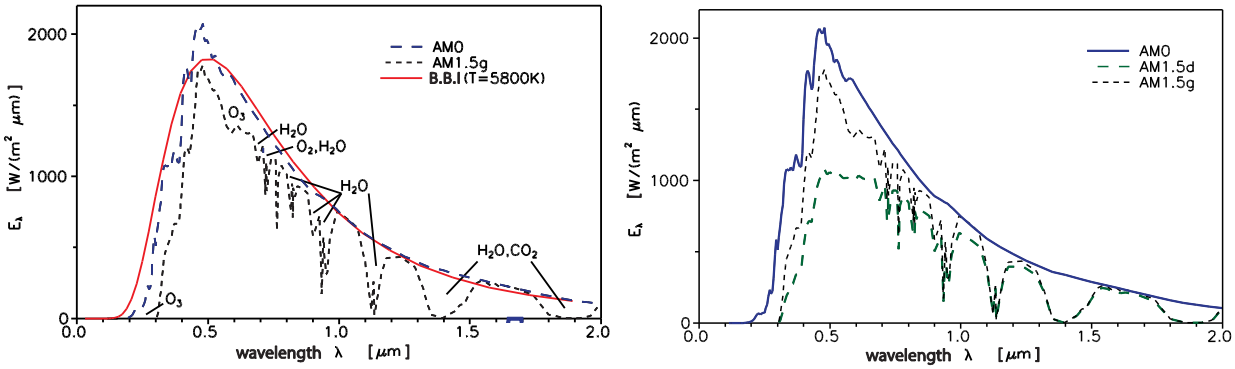

Figure 1: Spectral intensities of solar radiation. Atmospheric components responsible for several absorption lines are highlighted. AM0: radiation outside the atmosphere, AM1.5g: global radiation at air mass index 1.5, AM1.5d: direct radiation at air mass index 1.5, B.B.I.: black body irradiation [10].

Due to scattering effects in the atmosphere, one has to take into account that only a part of the global irradiation power originates from direct radiation, even at clear-sky conditions diffuse radiation contributes a significant part to the total irradiance onto a surface [9]. This is particularly important for concentrating photovoltaic technologies where only direct sunlight contributes to power generation.

$$I_{global} = I_{direct} + I_{diffuse}$$

2.1.3. Photocurrent generation

2.1.3.1. Light-matter interaction

As a photon hits a solid state body, it can either be reflected, transmitted or absorbed when transferring its energy to an electron. In a semiconductor most electrons are located in the valence band and are bond to the crystal lattice. The energy of the photon can now excite an electron to an energy level in the conduction band where it is free to move in the crystal lattice and therefore can contribute to electrical conduction. It leaves behind a hole, which can also contribute to conduction. Depending on the material, these electron-hole pairs can have binding energies holding them together, as electrons and holes attract each other by Coulomb forces, and can be described as neutral quasi-particles called excitons, which can also move around in the material. After a time excitons (or free electrons and holes) can recombine, therefore positive and negative charge carriers must be separated spatially to contribute to power generation. Electrons can only be excited to the conduction band by photons with an energy equal or bigger than the band gap energy.

$$W_{ph} = h\nu \geq W_G$$

W_{ph} is the photon energy, h the Planck constant, v the frequency and W_G the band gap energy. If the energy is bigger, the electron will relax to the band edge and dissipate the excess energy as heat. If the energy is lower, the photon will pass through the semiconductor, or in other words, the semiconductor is transparent for the photon [9, 10].

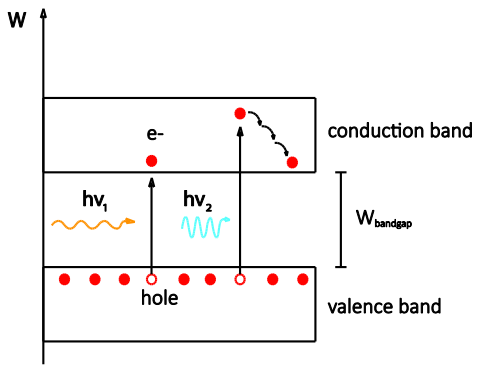

Figure 2: Schematic process of photon-induced electron excitation in a semiconductor.

The value of the intensity of light entering a solid state body with (or the number of photons not being absorbed) can then be described by the equation

$$I_{(x)} = I_0 * e^{-\alpha x}$$

Where x is the distance into the material, I_0 the intensity at the surface and α is the absorption coefficient, a material constant. From this a penetration depth x_E can be derived, for which the intensity has decreased to a value of 1/e:

$$x_E = \frac{1}{\alpha}$$

In a direct semiconductor, only the energy of the photon is crucial for the generation of an exciton, in an indirect semiconductor, the electron also has to change its momentum to change its state between valence band maximum and conduction band minimum. This requires additional phonon absorption or emission for creation and recombination of excitons [9]. For this reason, the probability for an electron transition in a direct semiconductor is higher, and the absorption coefficient is larger.

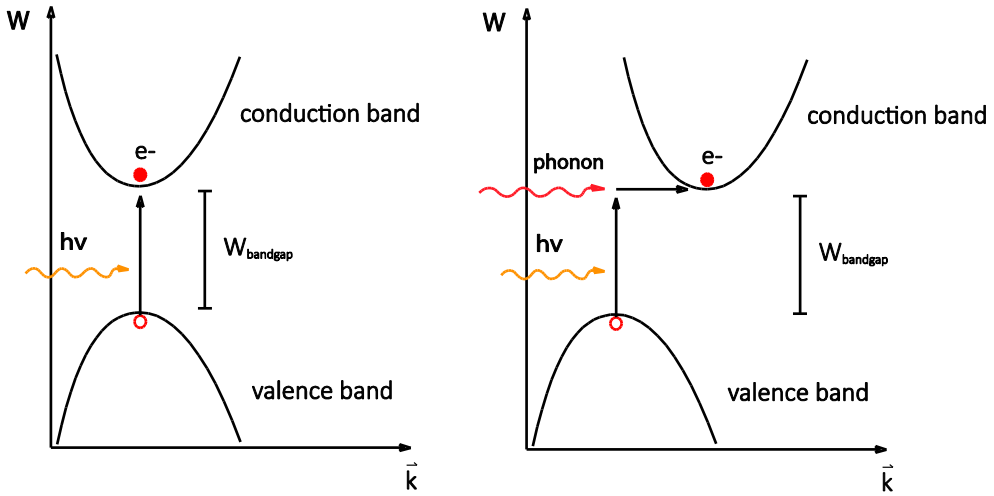

Figure 3: Schematic illustration of a direct and indirect band transition of an electron. The energies of the electron states is plotted over momentum k. The left picture shows a direct transition, the right picture shows an indirect transition including a photon and an additional phonon.

2.1.3.2. Charge carrier separation

To create an utilizable voltage in a solar cell it is necessary to successfully separate the photo-generated charge carriers. This is achieved most commonly via a p-n-junction.

Charge carriers move in a semiconductor either by thermal diffusion or driven by an electric field. When bringing an n-doped and a p-doped semiconductor into contact the excess charge carriers (electrons for the n-doped material and holes for the p-doped material) can diffuse into the other material. There, they recombine to fill up noble gas configuration, what creates charged ions because the initial materials have been neutral. This leads to the formation of a depletion region without mobile excess charge carriers, and the charged ions lead to a space charge zone i.e. an internal electric field due to the positive ions on one side and negative ions on the other side of the junction. This electric field also limits the diffusion at some point and leads to a stable depletion zone [9].

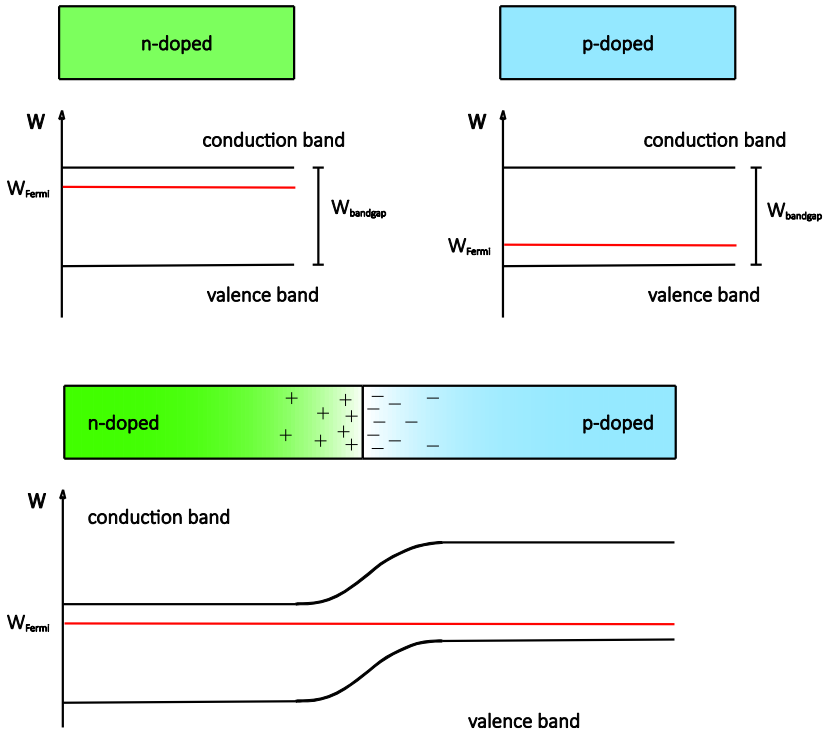

Figure 4: Schematic illustration of a p-n junction. The bands of the materials align in a way that the Fermi-levels in both materials are equal. The charge carrier exchange upon contact leads to a charged depletion zone at the interface.

This has an important effect on the electrical behavior of a p-n junction: When applying voltage to the junction in forward bias, i.e. injecting further electrons on the n-doped side and holes on the p-doped side, the depletion region is being reduced until current can flow over the junction. When applying reverse bias, the opposite is happening: extracting electrons of the n-doped side pulls them away from the junction and expands the depletion zone; no current can flow until the voltage is raised to a break-down voltage [9].

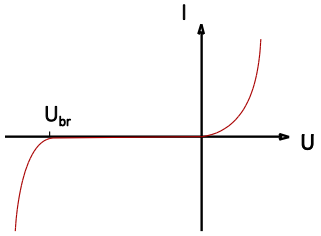

Figure 5: Characteristic curve of a p-n diode. U_{br} indicates the break-down voltage.

Upon illumination, generated charge carriers diffuse randomly in the semiconductor and are separated as soon as they reach the internal field of the p-n junction. This separation leads to a voltage which can be measured at the outer sides of the diode, the open-loop voltage.

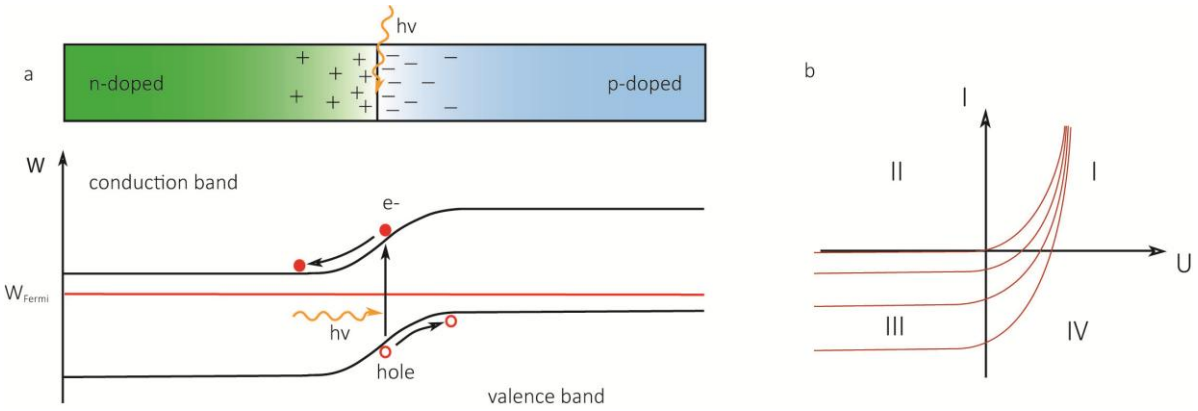

Figure 6: p-n junction upon illumination. a: illustration of the charge carrier separation process. b: characteristic curve of a photodiode. The 3rd quadrant represents the operational mode of a photodiode, the 4th quadrant the one of a solar cell.

With no light upon a photodiode, it behaves like an ordinary p-n junction: in reverse bias no current is flowing apart from a very small cutoff current also called dark current. Upon illumination, a bias-voltage independent photocurrent is added (in reverse direction). This operational mode is called photodiode, utilized for instance in light detectors. The operation in the fourth quadrant is relevant for solar cells: A negative current is flowing while a positive voltage is applying at the contacts, i.e. electrical energy is being produced by the device.

The characteristic curve of a photodiode is given by the equation

$$I = I_{PH} - I_D = I_{PH} - I_S \cdot (e^{\frac{U}{m \cdot U_T}} - 1)$$

I_{PH} is the photocurrent, I_D the diode current, which is determined by I_S, the saturation current, temperature voltage $U_T = \frac{kT}{q}$ and an ideality factor m typically between 1 and 2, adjusting the equation to real solar cells.

As all real solar cells are built of non-perfect materials, failure atoms are inherited in the crystal lattice. These atoms provide trap states in the band gap which promote recombination of the generated electron-hole pairs. Therefore the mean lifetime τ_n of charge carriers in the material as well as the diffusion L_n length become important parameters when characterizing a solar cell material [9] and is described by the relation

$$L_n = \sqrt{D_n * \tau_n}$$

with D_n being the material-specific diffusion constant. Diffusion lengths in crystalline silicon are typically up to 400 µm [17]. This is especially important for relatively thick solar cells, where generated minority carriers have to diffuse over greater distances until they reach the space charge zone.

2.1.4. Efficiency

Generally, efficiency of power conversion denotes the ratio of converted power to input power. In the case of a solar cell this is the electrical output power when operated at the cell's maximum power point in proportion to the incident light power:

$$\eta = \frac{P_{el}}{P_L}$$

Reflectance and quantum efficiency of the solar cell reduce the amount of light before irradiation energy can be converted to electrical energy. The external quantum efficiency denotes the amount of photons generating extractable electron-hole pairs N_{eh} in relation to the number of all incident photons N_{ph}:

$$\eta_{ext} = \frac{N_{eh}}{N_{ph}}$$

The internal quantum efficiency takes out reflectance or transmittance losses and solely describes the quantum conversion by

$$\eta_{int} = \frac{\eta_{ext}}{1 - R}$$

where R is the reflected or transmitted fraction of the incident light.

For planar solar cells made of a single semiconductor p-n junction W. Shockley and H. Queisser published an ultimate theoretical efficiency limit in 1961. In this work, reflection and transmission losses have been neglected and the external quantum efficiency set to be $\eta_{ext}=1$. Black body irradiance with a temperature of 6000 Kelvin was assumed for the spectral intensity. The base of the calculations is formed by black body radiation and absorption, as well as the fact that only photons with energies higher than the band gap of the active material can contribute to electrical power generation, but still only with the bandgap energy. The limit is calculated to be about 31% at a band gap of 1.3 eV [13].

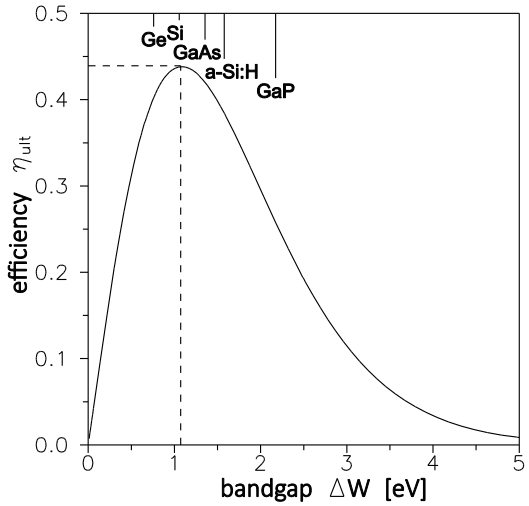

Figure 7: Ultimate efficiency limit for single junction PV cells plotted over band gap, values for different materials are noted above [10].

This limit however does not apply if the solar spectrum can be used more efficiently by combining several materials to a multi-junction cell. In this case, materials with larger band gaps are placed on top, absorbing only high-energetic photons and being transparent for longer wavelengths, followed by one or more layers of materials with lower band gaps beneath. Additionally to the better exploitation of the solar spectrum, electroluminescence of recombining charge carriers can again contribute to the power generation, although only to a small amount. A maximum efficiency limit was also published for this kind of cells by A. De Vos in 1979 and is calculated to be 42.3% for a two layer cell with band gaps of 1.9 eV and 1.0 eV, respectively. For three layers the theoretical limit is 49%, for an infinite number of layers 68.2%. If light is focused and concentrated onto a cell, the efficiency can be improved even more. With a concentration ratio of 45900, which is considered to be the highest concentration theoretically possible, a single layer cell would yield an efficiency of 40% and an infinite number of layers even 86.8% [18].

Of course these are theoretical limits, as for 2015 the efficiency record is reported to be about 46%, reached by a four-junction cell with a concentration factor of 508 [19]. One nevertheless has to keep in mind that these high concentration photovoltaics strongly depend on direct sunlight and therefore are suited only for specific regions, as well as they need two-axis sun-tracking systems to be mounted on.

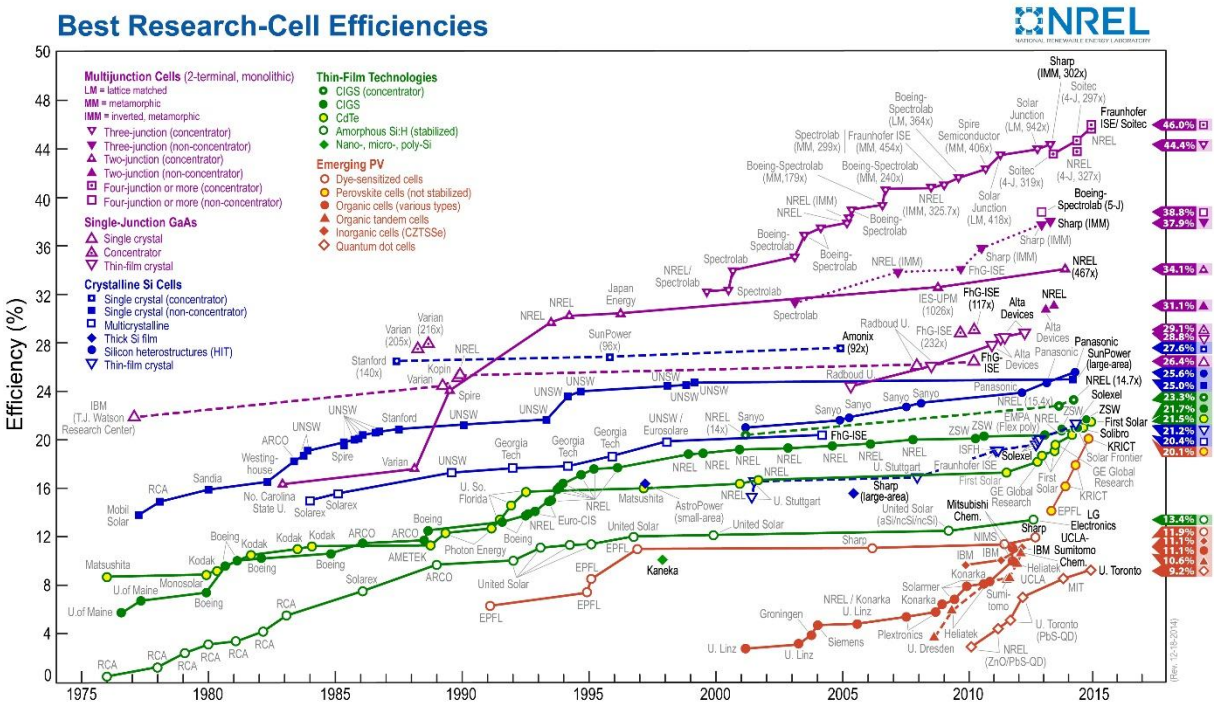

Figure 8: Development of the cell efficiencies for various cell types [20], compare [15].

When having a look at the characteristic curve of a solar cell, one can easily read out two important parameters: the short circuit current I_{SC} and the so-called open-circuit-voltage U_{OC}. The short circuit current is the maximum current a solar cell can deliver, flowing when bringing the two sides of the diode in direct electrical contact without a load connected, and therefore having no voltage drop between the contacts. The open-circuit-voltage is the maximum voltage a solar cell can deliver with no current flowing between the contacts. For power generation, the product of voltage and current is essential, which would be equal to zero at both the points I_{SC} and U_{OC}. Therefore an optimal operating point for the solar cell has to be found, which is referred to as maximum-power-point MMP, for which the extracted electrical power is given by

$$P_{MMP} = U_{MMP} * I_{MMP}$$

[9, 10]. The fill factor now describes the relation between the power that can be extracted at the maximum-power-point and the product of I_{SC} and U_{OC}.

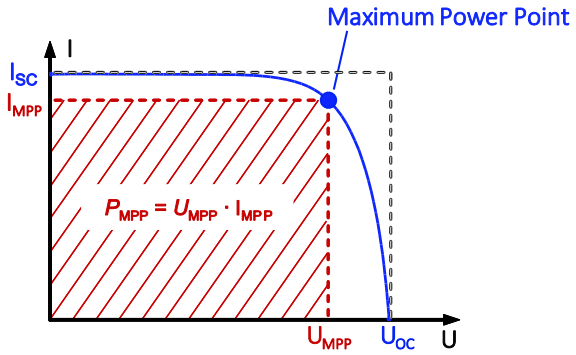

Figure 9: Maximum power point and fill factor: The fill factor describes the ratio of the maximum extractable power (red rectangle) to the product of I_{SC} and U_{OC} (black rectangle) [9].

2.1.5. Solar cell concepts

2.1.5.1. Single junction cells

The most spread solar cells used for common photovoltaic energy generation are made of crystalline silicon (c-Si). These include mono- and polycrystalline Silicon, the latter being cheaper in production but slightly inferior in efficiency. Reported top-efficiencies are in the range from 20% (polycrystalline cells) to 25% (single crystal) [15, 21]. In spite of the high effort of silicon production, these are the most established solar cell concepts because they have been developed since the 1950ies [12] and are generally more efficient than the next generation of solar cells – thin film cell solar cells [15].

Thin film solar cells, also referred to as second-generation photovoltaics, significantly reduce the amount of material necessary for the cell production. By the application of direct-bandgap semiconductors which have higher absorption coefficients, the use of thinner layers is possible. For a comparison: the penetration depth in crystalline silicon (indirect bandgap, 1.1 eV) is about 2.5 µm and in amorphous silicon (direct bandgap, 1.7eV) about 0.25 µm [9]. Several different materials have been involved in the development of thin film solar cells, including cadmium telluride (CdTe), Copper-Indium-Gallium-Diselenide (CIGS) and amorphous

silicon. Although the amorphous silicon technology is being outperformed by other technologies concerning efficiency, and the cells lack of long-term stability, there is still economical interest in this technology [15]. CdTe cells are being viewed controversially because of the toxicity of cadmium for the environment and the scarce availability of tellurium, which makes them being questionable as ecological solution for power generation. Nevertheless, they are being reported to have a high market share compared to other thin film technologies and comparably low production costs [15]. CIGS-cells used to be the most efficient commercial thin film technology, although their market share is lower than the one of other thin film technologies. Most recently, they have again been outperformed by CdTe cells concerning efficiency [22]. At last there are also gallium arsenide (GaAs) thin film solar cells to mention, which hold the record for thin film cell efficiency with 28.8%, though due to their high costs they are limited to extraterrestrial applications in their single junction thin film form [23].

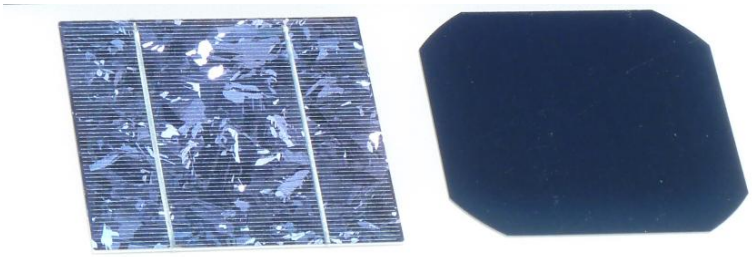

Figure 10: Silicon solar cells. To the left a polycrystalline cell, to the right a monocrystalline cell [24].

2.1.5.2. Multi junction cells

Multi junction solar cells consist of several thin films stacked on top of each other to absorb the solar spectrum more efficiently, for instance Ge/GaAs/$GaInP_2$. This yields efficiencies as high as 46% for concentrated sunlight [22]. Due to their high production costs they are mainly being used under concentrated sunlight so the cell area can drastically be reduced. This requires a high proportion of direct sunlight available at the chosen site as well as sun tracking mounts, so their application is limited to specialized usages [9].

2.1.5.3. Newer solar cell concepts

Organic solar cells are made of thin films of organic compounds such as polymers. A high absorption coefficient favors the design of very thin and flexible layers, and easy production processes without the need of cleanrooms, as well as inexpensive materials, seem promising for future developments [10]. The efficiency however does hardly match other cell types, [22] which is due to a more complex charge carrier separation process. Generated electron-hole pairs are bound in excitons with relatively large binding energies up to 0.4 eV and have short diffusion lengths of 5-10nm [10]. This led to the design of anisotropic bulk heterojunctions, where an organic donor and acceptor material are mixed thoroughly and short diffusion paths for the excitons to the junctions are established [10]. The current efficiency record of 2014 is about 11% in laboratory conditions [22].

Dye-sensitized solar cells also represent a new opportunity for low-cost solar cells. They are based on a photoelectrochemical process similar to photosynthesis. A porous layer of titanium oxide covered by a dye which absorbs sunlight acts as an electrode, and is immersed in an electrolyte with another electrode (platinum or graphite) at the opposite side. Charge separation only occurs at the surface between the dye, titanium oxide and the electrolyte [10]. Dye-sensitized solar cells are the most efficient of the so-called third generation solar cells with record efficiencies of 11.9% [22]. The major disadvantage of this cell technology is the use of a liquid electrolyte which is not temperature-stable, decomposes after time and can damage the cell itself physically [10].

2.1.5.4. Two-dimensional solar cells

Just recently, a photovoltaic effect in two-dimensional semiconducting materials (transition metal dichalcogenides) has been discovered [6–8]. A p-n junction consisting of two atomically thin semiconducting layers is created by stacking monolayers vertically on top of each other. Upon illumination, generated electron-hole pairs are separated instantly into the two layers

(they do not have to diffuse to the junction as the materials are two dimensional and all the overlap area can be regarded as the junction itself) and establish an utilizable potential difference [7].

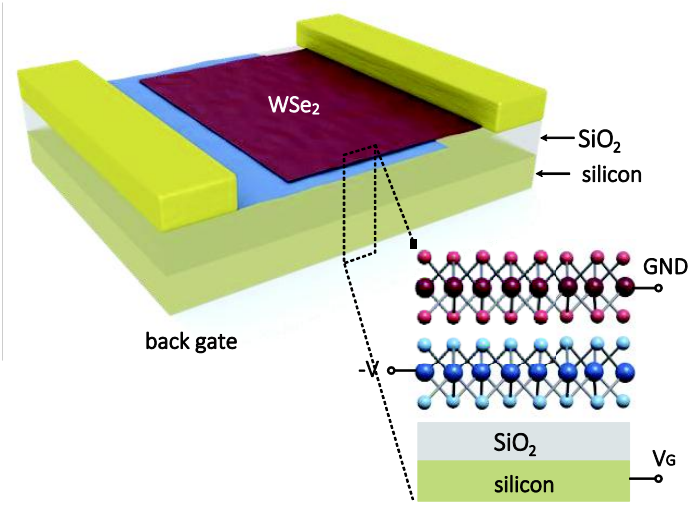

Figure 11: Schematic picture of a two dimensional heterojunction [7].

Two-dimensional materials exhibit extraordinary mechanical stability, allowing them to be used on flexible substrates for instance [25]. As two-dimensional materials consist of only one atomic or molecular layer, they are optically semi-transparent, absorbing up to 10% of the incident light [6]. This allows them to be used for semitransparent applications, for instance for application on windows or facades. At the same time they exhibit very large power densities of up to 2000 kW/kg (which would be about 1000-fold of conventional silicon solar cells), considering these materials are only fractions of nanometers thick and therefore extremely light weighted in relation to their expanse [6]. Efficiencies are reported to range from 0.1% to about 1% [6, 7], but considering the transparency of the devices, the low amount of material necessary for the fabrication of large area modules and the fact that this technology is still very new, a lot can be expected from it in the future.

The main limiting factor for efficiency in this kind of cells seems to be interlayer recombination of the generated electron-hole pairs, which shall be addressed within this work.

2.2. Transition metal dichalcogenides (TMDC's)

2.2.1. Solar cell concepts

Transition metal dichalcogenides (further referred to as TMDC's) are a group of materials which are of increasing interest within the research field of two-dimensional materials.

Since the discovery of graphene by Novoselov et. al. in 2004 [1] and the consecutive Nobelprize in 2010 [26] interest has grown in the research field of two-dimensional materials. Graphene itself has been the first material which was found to be existent as a two-dimensional material, a crystal with a thickness of just one atomic layer. This caused sensation because until that time, this class of materials was thought not to be stable under ambient conditions.

The crystal structure of these materials implies several distinctive mechanical and electrical properties which distinguish those materials in their two-dimensional form from their bulk counterparts and make them interesting for various applications [1, 4]. Graphene itself, lacks of a band-gap in its electronic structure, which makes it unsuitable for applications in which semiconducting properties are an essential requirement, as for instance for the design of transistors or optoelectronic devices [27].

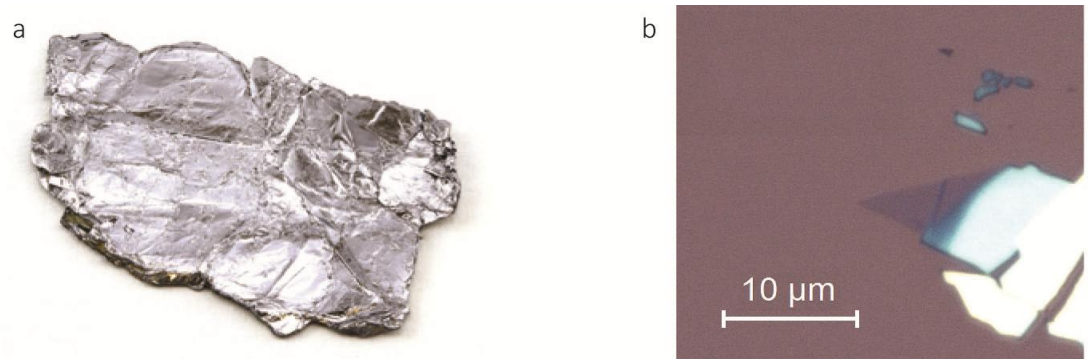

Figure 12: a: MoS_2 bulk crystal [28]. b: optical microscope picture of monolayer WS_2 flake [sample WS2-WDT-3_F6]

TMDC's include several materials which perfectly come up for this disadvantage and serve as excellent two-dimensional semiconducting materials with a wide variety of properties from which the materials can be chosen to exactly fit the needs of any intended application.

In their bulk form, TMDC's have been investigated in the last decades for their diverse properties such as lubricity, their semiconducting properties, magnetism and superconductivity just to name a few [29]. In their two-dimensional form they are lately being used to fabricate electronic devices, which due to their marginal thickness and mechanical stability can be designed on flexible and transparent substrates [30]. When reducing their thickness to monolayer, many group-six TMDC's show enhanced photoluminescence, which can be accounted to a change in the band structure [31]. This, in combination with their large carrier mobility, gate-tunability and strong light absorption make group-six TMDC's (e.g. built up of W or Mo) important tools for novel optoelectronic engineering [5, 28, 32, 33]. Further, it was shown that a single-layer TMDC absorbs up to 50 times more light than comparably thick Silicon and can be used for converting solar energy into electrical power, thus operating as a solar cell [6].

As graphite does, most TMDC's also consist of a layered structure with very strong in-plane bonds and comparably weak inter-layer bonds, which makes them easily cleavable into monomolecular layers and thus accessible for the processing of devices.

H																	He
Li	Be											B	C	N	O	F	Ne
Na	Mg	3	4	5	6	7	8	9	10	11	12	Al	Si	P	S	Cl	Ar
K	Ca	Sc	Ti	V	Cr	Mn	Fe	Co	Ni	Cu	Zn	Ga	Ge	As	Se	Br	Kr
Rb	Sr	Y	Zr	Nb	Mo	Tc	Ru	Rh	Pd	Ag	Cd	In	Sn	Sb	Te	I	Xe
Cs	Ba	La - Lu	Hf	Ta	W	Re	Os	Ir	Pt	Au	Hg	Tl	Pb	Bi	Po	At	Rn
Fr	Ra	Ac - Lr	Rf	Db	Sg	Bh	Hs	Mt	Ds	Rg	Cn	Uut	Fl	Uup	Lv	Uus	Uuo

Figure 13: Periodic table highlighting transition metals and chalcogens [33].

2.2.2. Chrystal structure

The atomical structure of TMDC's is of the type MX_2, where M represents a transition metal element of the groups 4-10, and X is a chalcogen [33]. There are now many possible combinations of those elements to form a TMDC, of which not all exist as two-dimensional materials.

As mentioned before, for a material to be cleavable and thus being able to extract monolayers, the in-plane bonds of the crystal must be comparably strong to the out-of-plane bonds. This is the case for most group 4-7 TMDC's, whereas most group 8-10 TMDC's normally only exist in non-layered structures [33]. The TMDC's not appearing in layered structured are only partly colored in Figure 13.

In the case of layered materials, each layer consists of a top and bottom sheet of chalcogen (X) atoms with a middle layer of transition metal (M) atoms in between. The intra-layer bonds between the M and the X atoms are mainly covalent, whereas the inter-layer bonds between the planes are of van-der-Waals character and comparably weak. Each layer has a thickness of about 6-7 Ångström and the unit cell of the crystal is either of trigonal prismatic or octahedral (also referred to as trigonal-antiprismatic) structure, depending on the combination of M and X elements and the history of the materials formation [33]. The layers in a bulk TMDC can then again form different stacking polymorphs with consecutive layers being in different phases, yielding a great variety of possible structural states [29]. For two-dimensional materials, this is of special significance when stacking different TMDC-monolayers to form a heterostructure, where different phases in different materials can be used to match lattices and thus form coherent electronic structures [34].

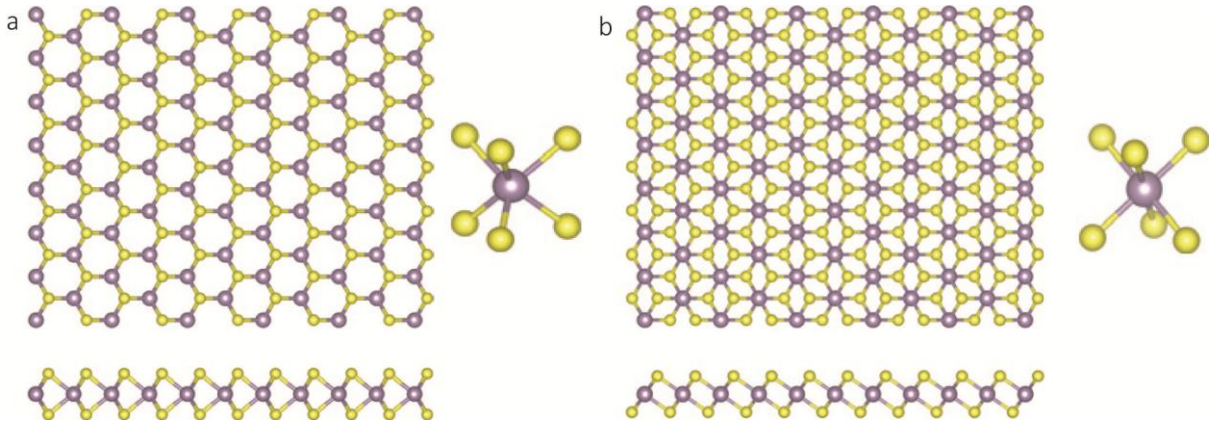

Figure 14: a: Trigonal prismatic and b: Octahedral or trigonal anti-prismatic structure. Blue spheres indicate transition metal atoms and yellow spheres indicate chalcogen atoms [33].

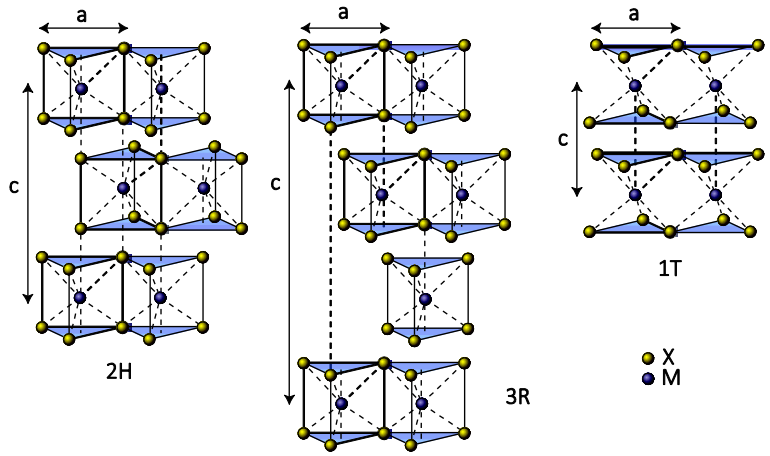

Figure 15: Different stacking polytypes of TMDC's. [28]

2.2.3. Synthesis of two-dimensional TMDC's

Generally, there are two approaches that yield TMDC's in their monolayer form: top-down and bottom-up methods.

Top-down methods include mechanical exfoliation, where a bulk crystal is mechanically cleaved until monolayers of the material remain [35]. In practice, soft adhesive materials are

used to cleave the crystal until few layers remain (therefore often referred to as the “scotch-tape-method”), which are then pressed onto a polished substrate. The monolayer flakes are then identified by optical microscopy and distinctive contrast values [36]. The resulting flakes exhibit high quality and therefore are ideal for research applications, but the obtained size of the flakes lies in the micrometer regime and therefore makes this approach unsuitable for large-scale applications.

Another top-down approach to fabricate single- or few-layer TMDC’s is liquid exfoliation. Several methods are provided here, for instance single layers of TMDC’s and other suitable materials can be produced by creating a dispersion of the crystal powder in organic solvents with compatible surface energies and then cleaving the material by ultrasonication [37, 38]. This method can be further enhanced by the introduction of intercalating agents, for instance lithium containing compounds [39]. Here, the lithium ions can intercalate between the layers of the TMDC materials, and as the TMDC is then exposed to water, the strong reaction between lithium and water cleaves the bulk material and yields to a large amount of very thin layers. The lithium-intercalation procedure can be controlled via an electrochemical process where lithium and TMDC crystals are used as electrodes [40]. Although these chemical exfoliation methods can yield large quantities of monolayer sheets up to several grams [41], the size of the flakes often remains in the sub-micrometer regime. Additionally, the lithium intercalation process causes structural changes in the TMDC crystal which can lead to a severe change in the materials properties. For instance, chemically exfoliated MoS_2 changes its electronic structure from semiconducting to metallic due to a transition of the crystal structure from the trigonal-prismatic phase to an octahedral phase, which can only partly be restored through additional annealing [42]. Also, the work with lithium compounds requires inert-gas atmospheres due to their flammability, and as the availability of lithium is limited, the development of alternative intercalating methods is necessary [28].

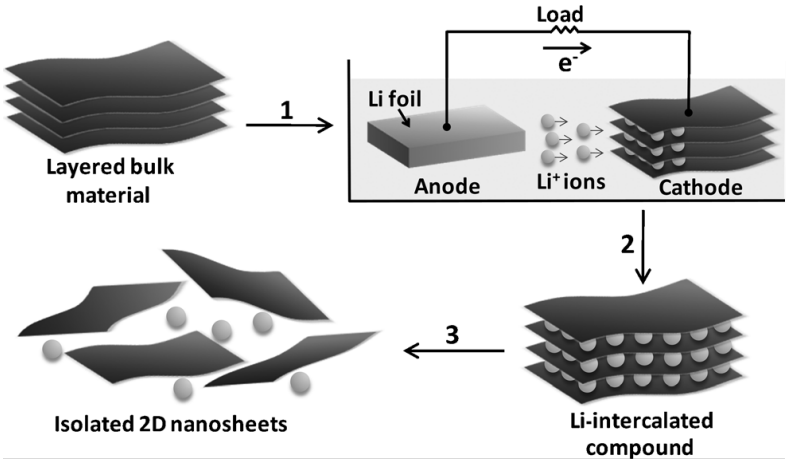

Figure 16: Schematics of the electrochemical lithiation process [40].

Bottom-up methods are generally aiming to grow single layers of the desired material onto a fitting substrate. Chemical vapor deposition (CVD) uses solid reactants; the desired transition metal and chalcogen elements (for instance MoO_3 and sulphur powder to yield MoS_2) which are then heated to high temperatures so that their vapors react, forming the desired TMDC on the surface of a substrate which is placed over the precursors (for instance SiO_2/Si, pretreated with reduced graphene oxide) [43]. The produced layers reach sizes of several square millimeters, but the thickness is dependent on the processing parameters, e.g. the concentration or thickness of the source material, and exact control of the layer numbers over large areas has not been achieved yet [28].

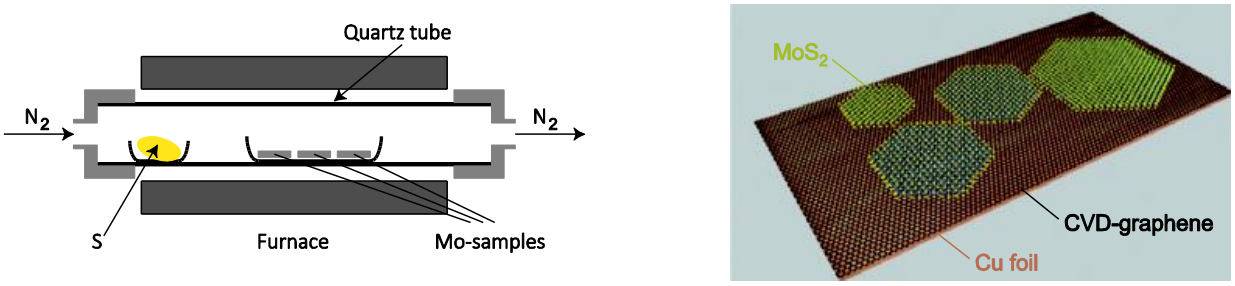

Figure 17: Schematics of the CVD growth of MoS_2 monolayers. [33]

Furthermore TMDC monolayer growth of for instance $MoSe_2$ has been achieved by molecular beam epitaxy (MBE) in ultrahigh vacuum onto a highly crystalline substrate which is for instance terminated with epitaxial graphene [44].

2.2.4. Electronic structure

The electronic structure of a TMDC is mainly dependent on the number of the non-bonding d-electrons of the transition metal and its crystal coordination structure [33]. Layered TMDC's crystallize in the trigonal-prismatic (2H) or octahedral (1T) coordination, group six TMDC's are most stable in the 2H phase, although the 1T phase can be induced through external influences like the intercalation of lithium ions as mentioned before [5]. TMDC's in the 1T-phase form degenerate d_{z^2,x^2-y^2} and $d_{yz,xz,xy}$ orbitals, in group-six TMDC's these are then only partially filled and thus they exhibit metallic character in this phase. In the 2H-phase the d-orbitals split into three groups: d_{z^2}, $d_{x^2-y^2,xy}$, and $d_{xz,yz}$, with a band gap between the first two orbital groups. In this case, the group-six TMDC's split orbitals are fully occupied which gives them semiconducting character [5, 33].

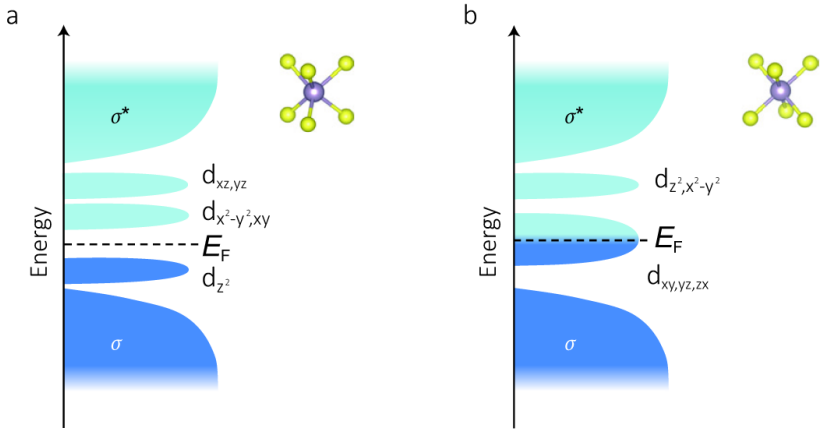

Figure 18: Orbital filling of a: Trigonal prismatic and b:octahedral or trigonal antiprismatic coordination of group-six TMDC's [33].

Further insight into the electronic structure needs energy dispersion to be taken into account and band structures can be calculated via first principle density functional theory (DFT) calculations. There are two valence band hills at the center (Γ) and the corners (K) of the Brillouin zone, and two valleys in the conduction band at the K-point and the Λ-Point [5]. The valence band at the K-point is split due to the effect of spin-orbit coupling and spin splitting [45] .

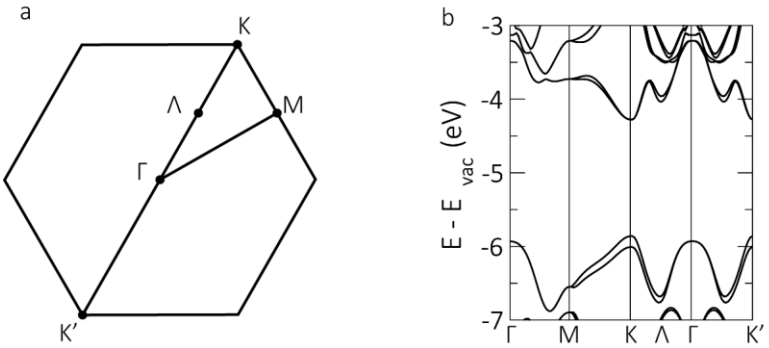

Figure 19: a: The hexagonal Brillouin zone of the TMDC crystal. b: Band structure with spin-splitting calculated from DFT calculations. b from [46].

A remarkable property of group-six TMDC's is the transition from indirect-gap semiconductors to direct-gap semiconductors when reducing their thickness from bulk materials to the monolayer limit [47]. This phenomenon gives rise to pronounced photoluminescence of monolayer group-six TMDC's and opens paths to potential light emitting applications [48–50]. This thickness-dependent effect is predominantly showing at the conduction band valley at the Λ-point and the valence band hill at the Γ-point. Analysis of the wave-functions at these points show that it consists of a mixture of the d-orbitals of the transition metal and the p_z-orbitals of the chalcogen atoms, which point to the direction of the outer surface of the TMDC-layer. Therefore this effect can not only be accounted to electron confinement but also to the interaction of the p_z-orbitals of the chalcogen atoms to the neighboring layers [5] .

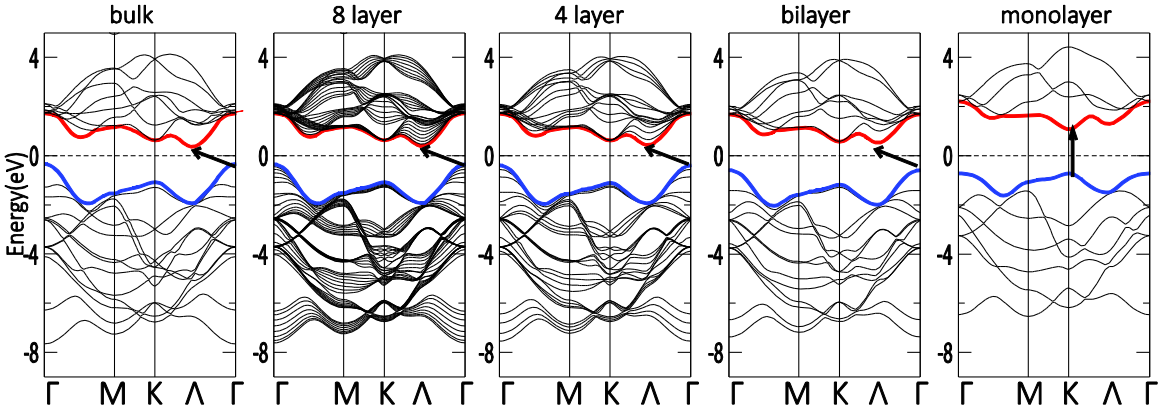

Figure 20: Comparison of the band structures of MoS2 with varying thickness and display of the indirect to direct band gap transition [47].

The calculation of absolute band gap values is dependent on accurate approximation models for the density functionals and the values given in literature differ and don't always match experimental values. In the following, an overview of calculated and experimental band gap values from literature of the TMDC's used in this work is given.

		Calculated values	Experimental values
MoS_2	Monolayer	1,89 eV [47] 1,91 eV [51] 1,9 eV [52] 1,58 eV / 2,01 eV [2] [46] 1,59 eV / 2,02 eV [2] [53]	1,89 eV [54] 1,87 eV [55] 1,85 eV [50]
	Multilayer	1,2 eV [52] (bulk)	1,3 eV [54] (bulk)
$MoSe_2$	Monolayer	1,58 eV [47] 1,66 eV [51] 1,33 eV / 1,72 eV [2] [53]	1,58 eV [44]
	Multilayer		1,41 eV [44] (8 layers)
WS_2	Monolayer	2,05 eV [47] 2,1 eV [52] 1,5 eV / 1,9 eV [2] [46] 1,55 eV / 1,98 eV [2] [53]	3,01 eV [56] 1,95 eV [48] 2 eV [31]
	Multilayer	1,3 eV [52] (bulk)	1,3 eV [48] (bulk) 1,45 eV [31] (5 layers)
WSe_2	Monolayer	1,61 eV [47] 1,25 eV / 1,63 eV [2] [53]	2,63 eV [56] 1,64 eV [55] 1,7 eV [31]
	Multilayer		1,4 eV [31] (5 layers)

Table 1: Calculated and experimental band gap values found in literature. The values given for multilayers refer to indirect band gaps whereas the values given for monolayers always are direct band gaps. Recent reports suggest that the real bandgaps are much larger due to large exciton binding energies which have been neglected in most of the given measurements and calculations [56].

[2] Different values given depending on the applied model for the densitiy functional: Perdew- Burke-Ernzerhof (PBE) versus Heyd-Scuseria-Ernzerhof (HSE), see [46] or [53] for further information.

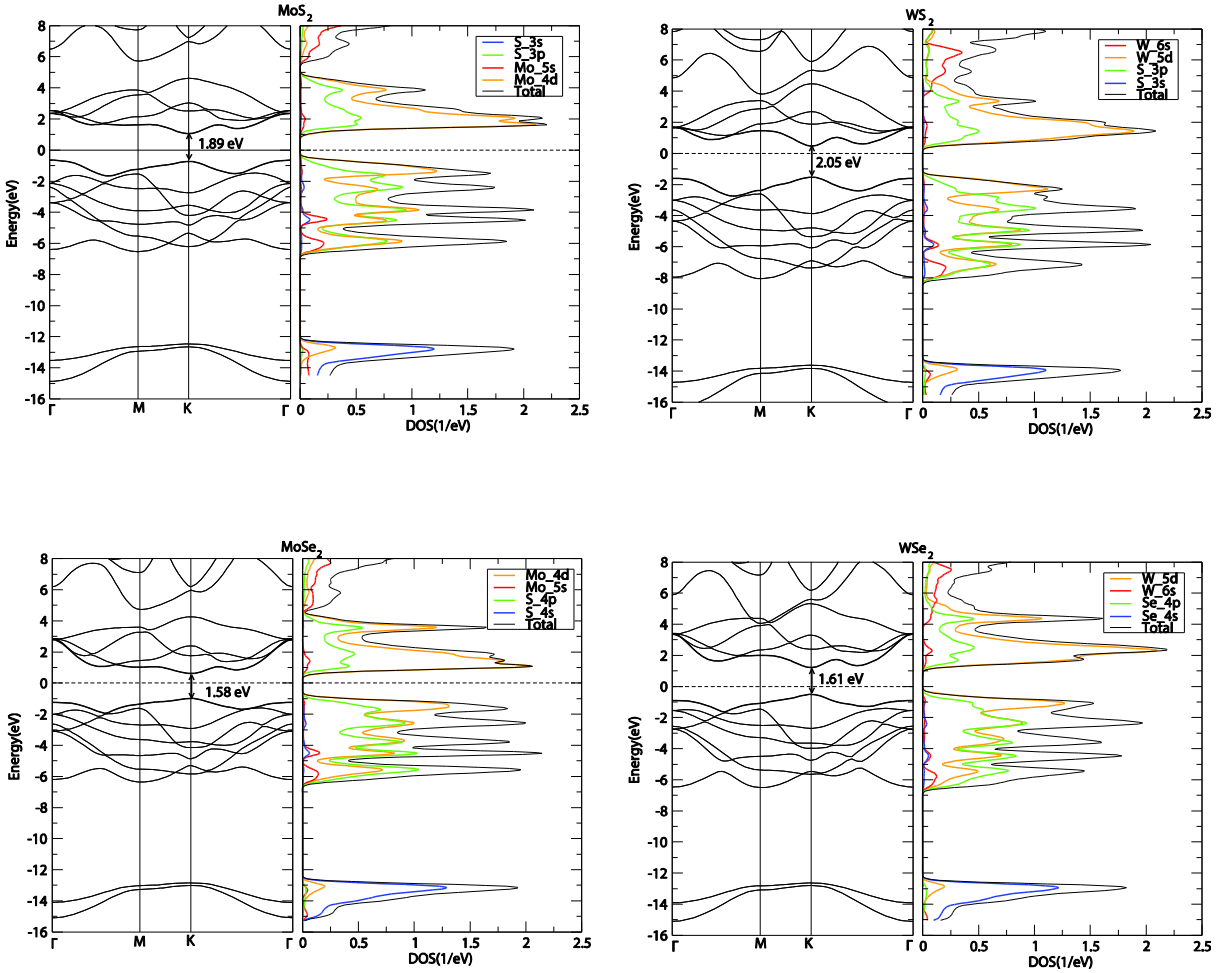

Figure 21: Calculated band structures with according density of states for the group-six TMDC's used in this work [47].

Within the time of writing Hanbicki et. al. [56] reported on large exciton binding energies in WSe_2 and WS_2 monolayers in the range of almost 1 eV which have been neglected in previous measurements and calculations. They suggest real band gaps therefore to be underestimated by about this value.

As the band structure changes with varying layer number, the electronic properties also change under applied strain, or in other words by altering the lattice constants of the material [30, 57]. Generally, a decrease in the band gap size is appearing under applied strain, which can be observed as a red-shift in photoluminescence spectra of the studied material [30].

Also, the appliance of an external electric field modifies the electronic properties and a transition to metallic behavior can be induced. This can be utilized to build monolayer TMDC field effect transistors with high current on/off ratios and very low standby power dissipations [58].

2.2.5. TMDC heterostructures

The high in-plane stability and the low van der Waals binding to neighboring layers allows TMDC monolayers to be restacked and combined with other materials to form new artificial materials with novel properties, referred to as van der Waals heterostructures [32]. The possibilities for creating new materials opened by this principles are nearly unlimited, which allows to build novel electronic and optoelectronic devices at the ultimate thickness limit, as for instance memory devices or solar cells [59]. In a first step, atomically sharp p-n-junctions from two materials (i.e. MoS_2 and WSe_2) were fabricated, exhibiting diode-like character under appropriate external electric fields (gate biases) and a photovoltaic effect under illumination [7, 8].

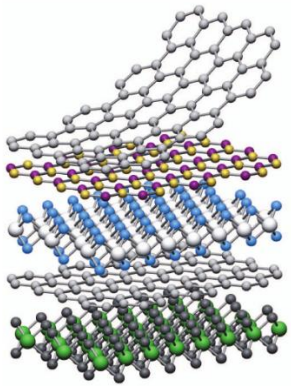

Figure 22: Schematic principle of building van der Waals heterostructures by stacking monolayers of different materials [32].

The electrical properties of the van der Waals heterostructures generally differ from those of their incorporated materials in their isolated monolayer form, because the interaction of the monolayers induce significant alterations to the bandstructure.

The heterostructure of MoS_2 and WS_2 monolayers is predicted to have an indirect band gap in contrast to the isolated monolayers, which is also decreased in size [6]. According to Bernardi et. al. [6], this is due to the interaction of the sulphurs p_z orbitals, leading to an increase of the valence band maximum energy at the Γ point. The valence band maximum at the K point is contributed by WSe_2 while the conduction band minimum originates from the MoS_2 layer. Upon illumination, this leads to the spatial separation of a photon-generated electron-hole-pair, where an electron changes from a state localized in the MoS_2 layer into a state in the WS_2 layer [6, 46]. This effect suggests a type-II-alignment of the semiconductors where MoS_2 works as acceptor and WS_2 as a donor, which allows this structure to operate as a solar cell.

Similar band alignments are being calculated for hetero-bilayers of $MoS_2/MoSe_2$ and MoS_2/WSe_2, though the latter is the only one to maintain a direct band gap, all others are predicted to undergo a transition towards indirect band gaps when stacked to heterostructures [60]. Due to the decreased band gap in the hetero-bilayers compared to the monolayers, the appliance of minor tensile strain (4-8%) or an external electric field can induce a semiconductor-to-metal transition of the stacks [60].

Because of the weak van der Waals interaction between the layers the lattice mismatch of the different materials can not be compensated, therefore a coherent structure will not be established and a Moiré-pattern will be formed [61]. By reason of this lattice mismatch also additional strain can apply to the individual layers as they are forming “bubbles”, which again influences the electronic structure by reducing the band gaps [51].

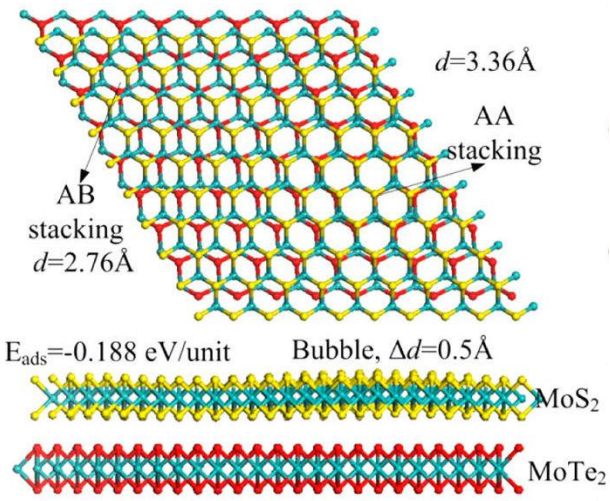

Figure 23: Moiré pattern of stacked TMDC's leading to the formation of bubbles and inducing strain to the lattice [51].

3. Fabrication and methodology

3.1. Exfoliation

In this work, TMDC thin films for building heterostructures were produced via mechanical exfoliation. Because the materials of interest consist of a layered structure with weak van der Waals forces holding the crystal layers together, they can easily be cleaved down to few or single layers by mechanically breaking up this weak bonds [35]. The advantage of mechanical exfoliation compared to other methods like chemical exfoliation or the growth of layers by chemical vapor deposition is the high quality and cleanliness of the obtained thin films, which is most important for fundamental characterizations [28].

The TMDC crystals cleaved to obtain monolayers were all of synthetic origin, except for MoS_2. Molybdenum disulfide occurs naturally and was purchased from the company "SPI" who acquires it from mining sites in Canada. It is further examined by them and guaranteed to exhibit purity of >99% [62]. $MoSe_2$, WS_2 and WSe_2 originate from different companies and are all synthetically fabricated, with guaranteed purities of >99.99% [63–65].

The substrates on which the flakes are deposited are single crystal silicon wafers of 350 µm thickness covered by 90 nm or 280 nm dry thermal oxide and polished to <100> crystal orientation on one side, purchased from the company Si-Mat Silicon Materials [66]. The wafers were cleaved to square pieces of about 1 cm edge length and thoroughly cleaned before usage. The cleaning process included ultrasonication in an acetone bath and in hydrochloric acid, followed by rinsing in isopropanol, blow drying with nitrogen and annealing on a hotplate heated to 120 °C.

Exfoliation itself proceeds as follows: The bulk crystal is pressed onto a strip of adhesive tape and peeled off again. This cleaves the crystal to an arbitrary thickness and leaves behind several small pieces of the TMDC material. A second piece of tape is then pressed onto the first and slowly withdrawn again, leading to further cleavage of the material. This step can be repeated a few times, until the crystal pieces are noticeably thinned, what can be optically recognized by examination in backlight. The tape is then brought into contact with the silicon

substrate, very light pressure is applied to establish full contact of the TMDC flakes and the substrate, and then the tape is again slowly peeled off. This leads to a final cleavage and van der Waals forces bind thin layers of the TMDC material to the silicon dioxide.

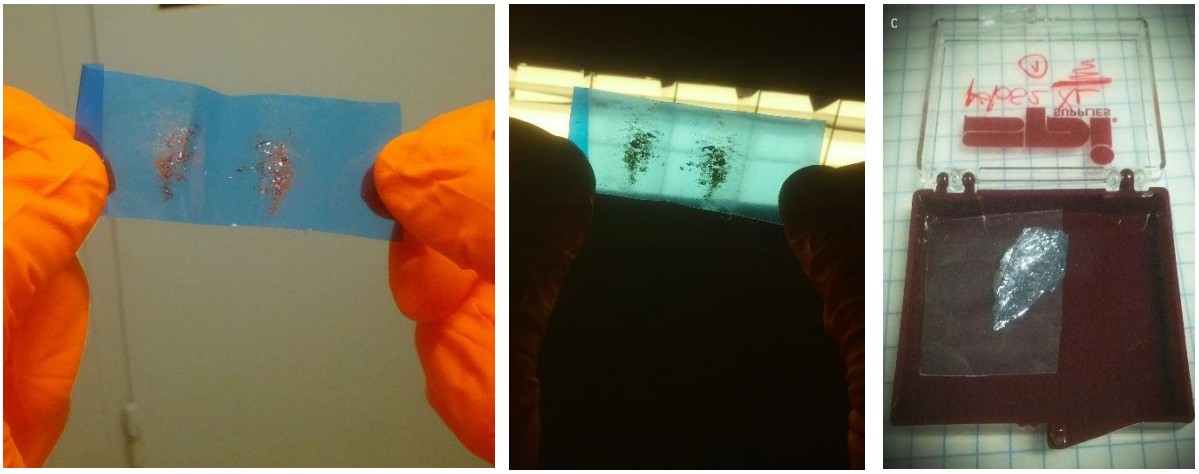

Figure 24: TMDC exfoliation. a: a strip of wafer dicing tape with MoS_2 after the first cleavage. b: backlight inspection. c: The MoS_2 bulk crystal.

Different parameters for this process were varied to obtain optimum results, with parameters varying slightly for different materials.

Two different adhesive tapes were used, commercially available scotch tape and wafer dicing tape. Scotch tape provides good adhesive properties and the tape itself is stiff and inductile, which empirically proved to be good parameters to yield flakes of an utilizable size. Although the disadvantage of this tape is that it leaves behind lots of glue residues, making optical search and characterization of flakes in the following steps challenging, as well as cleanliness of the obtained flakes no longer can be guaranteed.

Therefore wafer dicing tape was tried, which is optimized to leave a minimum amount of residues on the substrate. The disadvantage of this tape is its ductility; when peeling the tape slowly off the substrate (which involves a certain amount of strain applied to the tape), the tape stretches, leading to wrinkles and causing TMDC flakes to rip into tiny pieces. Therefore most of the flakes found on the substrates exfoliated by wafer dicing tape were too small for further utilization.

A solution could be found by combining the good properties of both materials: a strip of scotch tape was applied on the back side of the wafer dicing tape, giving the tape the desired stability and inductility maintaining the cleanliness of the wafer dicing tape.

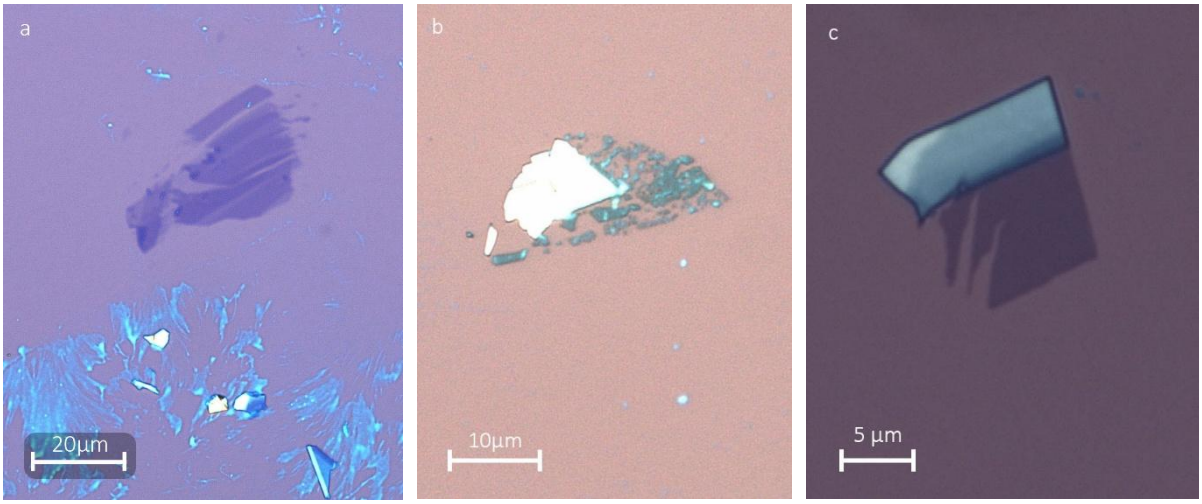

Figure 25: Results of different exfoliation methods. a: flake exfoliated with scotch tape, surrounded by glue residues. b: flake exfoliated with wafer dicing tape, ripped to tiny pieces. c: flake exfoliated with a combination of scotch tape on the back of a wafer dicing tape strip, yielding good results.

Nevertheless typical flake sizes rarely exceeded 5-10 µm in one dimension, and for the following stacking of the flakes bigger sizes were desirable. Hence a new exfoliation method based on a flexible polymer was tested. Polydimethylsiloxane (in the following referred to as PDMS) is a silicon based elastomer with velocity dependent adhesion properties, and can therefore be used as a stamp for controlled pickup and deposition of nanomaterials [67, 68]. The softness and flexibility of sufficiently thick PDMS allows it to perfectly adapt to the surface of the TMDC crystals, minimizing strain on the flakes and therefore reducing effects which are negatively influencing the yielded flake size, e.g. breaking, ripping and folding of the flakes. To fabricate the PDMS elastomer, a liquid PDMS base was mixed with a curing agent[3], centrifuged[4] at 6000 rpm to remove voids, poured onto a silicon wafer and subsequently cured on a hot plate for several hours. The silicon wafer had been prepared with an additional layer

[3] Sylgard 184 silicone elastomer kit, obtained from Dow Corning [83]
[4] Hettich Zentrifugen, EBA 20, [84]

of photoresist[5] to prevent tight sticking of the PDMS to the silicon wafer and at the same time enabling it to form a smooth surface. The photoresist was applied using a spin coater at 9000 rpm, annealed for 2 minutes at 120 °C, yielding a thickness of ~1µm [69]. The exact parameters of mixing ratio, PDMS film thickness as well as annealing time and temperature have direct influence on the viscoelastic properties of the yielded PDMS. At a ratio of 10:1 and a curing time of 6 hours at 60°C, PDMS films of ~2 mm thickness were produced with satisfying consistency. For exfoliation the TMDC crystals were cleaved off the bulk piece only once by a wafer dicing tape and then transferred to the PDMS stamp, where they were cleaved further and finally transferred onto the silicon substrate. Due to the velocity dependent adhesion of PDMS, it is possible to purposely pick up material by fast peeling and depositing material off the PDMS by slow peeling speeds [68]. Indeed huge flakes of up to 50 µm length and more could be obtained, although the total yield number of the flakes was very low.

Unfortunately, it later turned out that PDMS leaves residues of uncured oligomers on the surface of the TMDC flakes, which led not only to contamination and presumable tampering of the measurements, but also to severe problems in the stacking process. In the last step of the stacking process a polymer has to be dissolved, and PDMS residues trapped between the stacked TMDC layers react vigorously with the solvent ripping the precisely stacked flakes apart and destroying the sample. To overcome this problem, treatment of the PDMS in oxygen plasma as reported in [70, 71] was tried, which leads to enhanced crosslinking of superficial oligomers and to decreased contamination. However, this effect is not stable over time, and the surface recovers its original state due to the diffusion of free oligomers [71]. At the same time, adhesion was found to be drastically reduced at the treated surfaces and no utilizable flakes could be found.

Therefore this method of exfoliation was judged unsuitable for the production of TMDC heterostructures and was discarded for further experiments. In the following, flakes were again produced by the previously described method combining wafer dicing tape and scotch tape.

[5] AZ 5214 photoresist [85]

a b

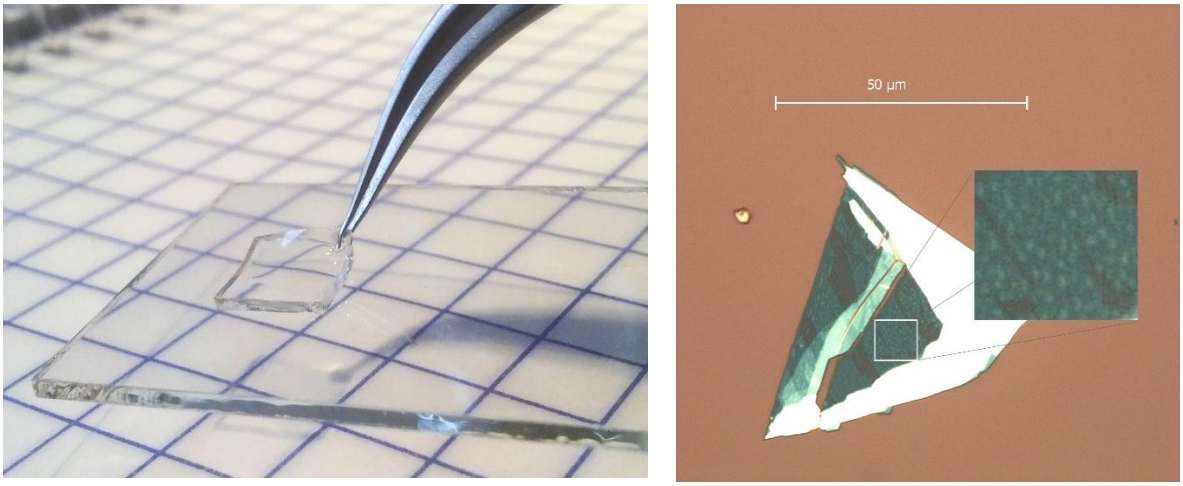

Figure 26: a: PDMS stamp being applied to a microscope slide. b: MoS_2 Flake exfoliated with PDMS, clearly showing PDMS residues on the surface.

3.2. Microscopy

Once the TMDC flakes were deposited on the silicon substrate, the samples had to be inspected optically and searched for mono- and/or fewlayer flakes. This was done via optical microscopy using a Leica DM6000. Utilizable flakes were approximately in the size of 5-10 µm, and could be recognized upon distinct contrast values.

The silicon substrate is covered by an oxidized layer with a thickness of 280nm, which proves to be the perfect thickness for enhancing the optical contrast of thin TMDC layers: [36] The reflectance of thin films (the TMDC layer and the oxide layer) on top of a semi-infinite substrate (silicon) can be calculated as

$$R(n_1) = \left| \frac{r_1 e^{i(\varphi_1+\varphi_2)} + r_2 e^{-i(\varphi_1-\varphi_2)} + r_3 e^{-i(\varphi_1+\varphi_2)} + r_1 r_2 r_3 e^{i(\varphi_1-\varphi_2)}}{e^{i(\varphi_1+\varphi_2)} + r_1 r_2 e^{-i(\varphi_1-\varphi_2)} + r_1 r_3 e^{-i(\varphi_1+\varphi_2)} + r_2 r_3 e^{i(\varphi_1-\varphi_2)}} \right|^2$$

with

$$r_i = \frac{n_{i-1} - n_i}{n_{i-1} + n_i} \qquad i = 1 \dots 3$$

being the relative refractive indices and

$$\varphi_i = \frac{2\pi d_i n_i}{\lambda} \qquad i = 1 \dots 3$$

the phase shifts due to optical path changes. The contrast between areas with and without flakes (n_1=1) can then be calculated as the relative reflectance

$$C = \frac{R_{(n_1=1)} - R_{(n_1)}}{R_{(n_1=1)}}$$

Hence, an optimum configuration can be found for every material. For thin TMDC layers the optimal SiO_2 thicknesses is approximately 90 nm and 270 nm [36].

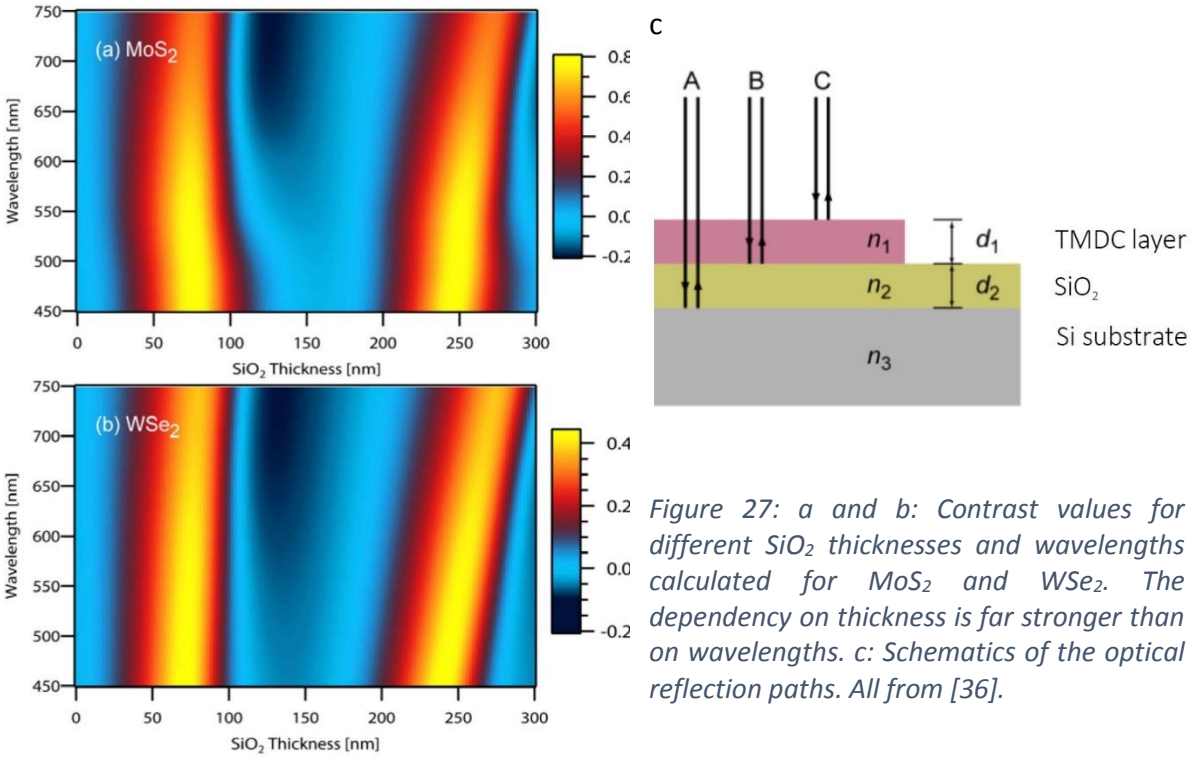

Figure 27: a and b: Contrast values for different SiO_2 thicknesses and wavelengths calculated for MoS_2 and WSe_2. The dependency on thickness is far stronger than on wavelengths. c: Schematics of the optical reflection paths. All from [36].

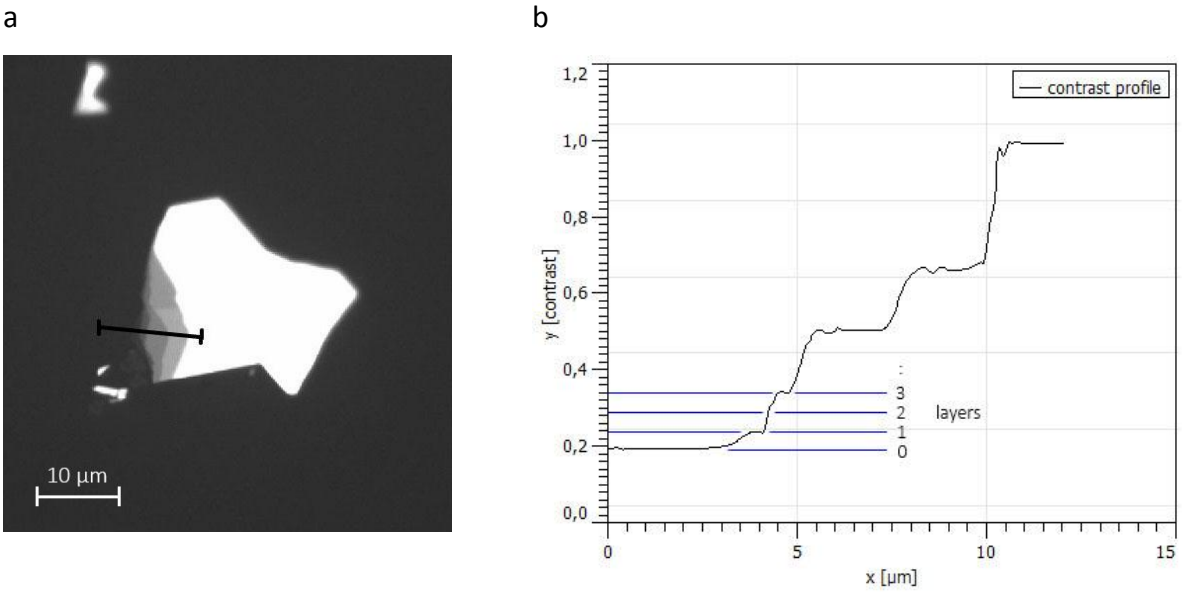

Figure 28: Contrast profile (b) extracted from (a) the optical microscope image (indicated by the black bar). As the contrast goes linearly with the layer thickness for the first few layers [72], step sizes clearly indicate layer steps (highlighted by blue lines).

3.3. Stacking

In order to form TMDC heterostructures it is necessary to precisely align and place flakes on top of each other. Under a microscope attached to a digital camera[6], flakes are aligned via a three-axis micromanipulator stage, allowing micrometer precise control. The top layer flake is exfoliated onto a transparent elastic stamp which itself is placed on a glass microscope slide. The slide is then mounted face down onto the micromanipulator and placed under the microscope. A sample with the consecutive flake is placed and fixed beneath the stamp, which in the following has to be accurately aligned via the micromaipulator. Lenses with large working distances are required in order to be able to switch between the focus planes of the stamp surface and the underlying sample. The stamp is then brought into contact with the underlying flake and raised again picking up the target flake. This turned out to be the crucial and most difficult step to successfully assemble TMDC heterostructures. Different stamp

[6] Canon EOS 100D digital camera

techniques for pickup and deposition were tested, as reported in the following. The pickup step can in principle be repeated as often as desired, enabling the fabrication of heterostructures with an arbitrary number of layers, although considering a certain failure rate at every step a reliable stamping method and precise control of the process are required for successful stacking. In a last step, the created stack is put down onto the last flake and deposited there, depending on the stamp, this can be achieved in different ways.

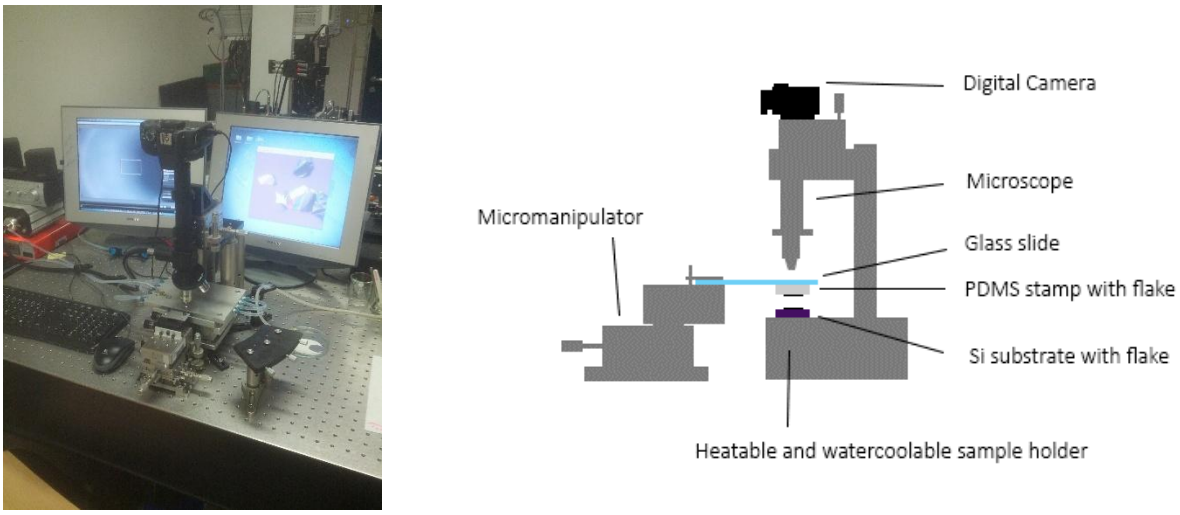

Figure 29: Picture and schematics of the stacking setup.

In a first step, PDMS with its velocity-dependent adhesion properties has been utilized to serve as a stamp for selective pickup and deposition of flakes, as reported in [73]. At high peel velocities, PDMS exhibits high adhesion forces, allowing to pick up material from a donor substrate. When lifting PDMS very slowly, the adhesion forces to the substrate are comparably higher and material from the stamp can be deposited [68]. The exact parameters of the critical peeling velocity strongly depend on the properties and thus the fabrication of the PDMS stamp. Highly cured PDMS exhibits generally lower adhesion, leading to difficulties within the pickup process, whereas less cured and therefore stickier PDMS alters its properties with time considerably, making reproducible results difficult. Due to the design of the stacks, the flakes to be picked up overlapped to the major extent of their surface with the flakes above and thus not directly get in contact with the PDMS itself, making velocity controlled pickup even more

difficult. The existence of PDMS residues on the surface of the flakes additionally contributed to the necessity of finding alternative transfer methods.

Another method was found by adding an additional layer of a thermoplastic polymer (polypropylcarbonate, in the following referred to as PPC) onto the stamp [74]. PPC granulate was dissolved in chloroform and dripped onto a glass slide to form thin layers after evaporation of the chloroform. The topmost TMDC layer of the planned stack was in the following exfoliated directly onto the PPC and examined on an optical microscope. Exfoliation onto heated PPC led to bigger flakes; due to the PPC's thermoplastic properties it gets soft upon heating and crystals nestle better to its surface without breaking. The PPC films were then manually lifted off the glass slides and placed on the PDMS stamps, serving as soft carrier material and again mounted on a glass slide. The stamps were subsequently aligned the same way as described before, but after bringing the flakes into contact, the donor substrate was heated to 65° C, again softening the PPC and establishing tight contact between the flakes and to the PPC. Before lifting the stack again, the substrate was cooled down to 15° C, hardening the PPC and fixing the embedded flakes yielding a high pickup rate. After placing the stack onto the third flake, the substrate was heated to 100° C, melting the PPC completely and allowing to separate the glass slide with the stamp from the flakes. The residual PPC embedding the stack has in the following been dissolved in chloroform. As mentioned before, stacks fabricated of flakes that had been exfoliated with PDMS were ripped apart by the strong reaction of the PDMS residues with the chloroform, but stacks made of classically exfoliated flakes stayed perfectly unaffected by this processing step, yielding a clean TMDC heterostructure.

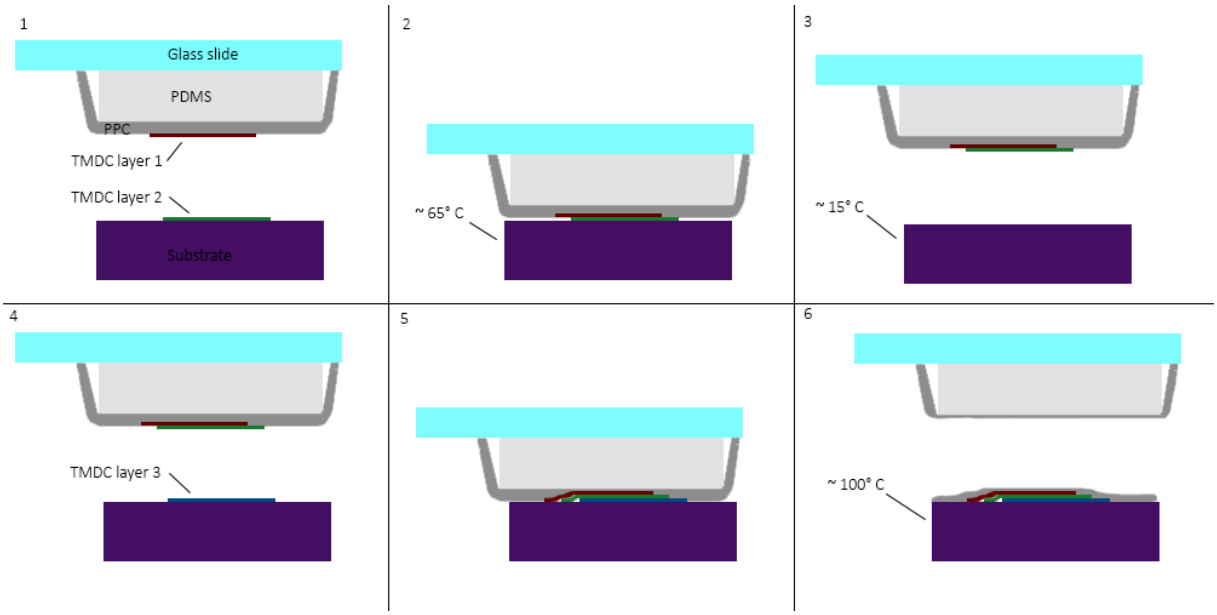

Figure 30: Schematics of the stacking process described in the text.

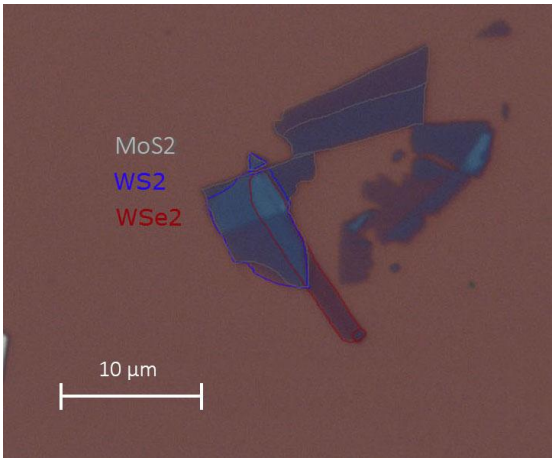

Figure 31: Stacked triple heterojunction consisting of MoS_2, WS_2 and WSe_2 (top to bottom). Flakes indicated with colored lines. Sample 20150109_1.

3.4. Contacting

Electrical contacts enabling characterization of the prepared TMDC heterostructures were created via electron beam lithography[7] and electron beam physical vapor deposition[8].

After looking at the samples in a scanning electron microscope (SEM, integrated in the Raith e-line) and defining markers for the alignment of the contact mask, the samples were coated with polymethylmethacetat (PMMA[9]) which serves as positive electron beam resist. Back in the e-line chamber, the designed mask had to be realigned to the device and finally the contact structures could be written onto the PMMA. After development and a stopbath, the contact mask is finished and can be examined by optical microscopy to verify the success of the process. The recipe used for this process (spin coating PMMA at 4000 rpm for 35 seconds, development of 45 seconds and a stopbath of 30 seconds), yields overhanging edges of the contact mask, which facilitates the lift-off of the mask after metal deposition [75, 76].

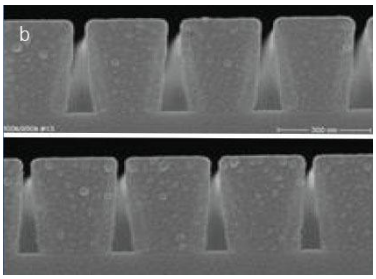

Figure 32: a: picture of the e-line writer in the cleanroom of the ZMNS at TU Vienna. b: Cross-section of structures written on PMMA with clearly overhanging edges. See [75].

[7] Raith e-line [86]
[8] Leybold electron beam evaporation chamber
[9] Positive PMMA E-Beam Resists AR-P 679.04 [75]

In the next step, the samples were inserted into a Leybold electron beam evaporation chamber for physical vapor deposition of the contact metals. In a high-vacuum chamber (pressure $<10^{-6}$ mbar) an electron beam was focused onto the target metals, heating them up and leading to their sublimation into the chamber. The sample has been placed face-down above the target and was evenly coated by the evaporated metal. The growth rate was monitored by an oscillating quartz crystal and is typically about 0.5 Å/s – 1 Å/s, yielding sufficiently low grain size and dense metal layers [77].

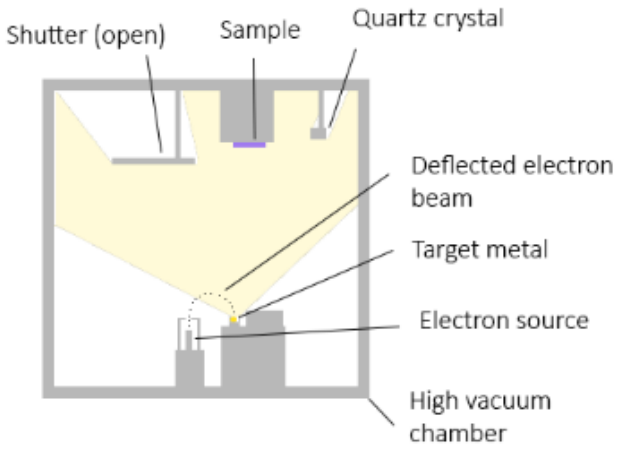

Figure 33: Schematics of the Leybold electron beam evaporator. Light yellow indicates metal vapor.

The contact materials were chosen as follows: at the bottom 5 nm of chromium were deposited, which served as an adhesion layer for following materials but did not fully cover the surface due to island growth [78, 79]. A consecutive layer of 40 nm of palladium was deposited, which actually was supposed to serve as the contact material due to its fitting work function. Another layer of 60 nm of gold was deposited on top to reinforce the contact pads, yielding a total thickness of 105 nm.

As a final step, the samples were placed in an acetone bath for several hours to dissolve the PMMA contact mask and lift off the evaporated metal upon it, leaving behind only the TMDC heterostructure with the produced contacts.

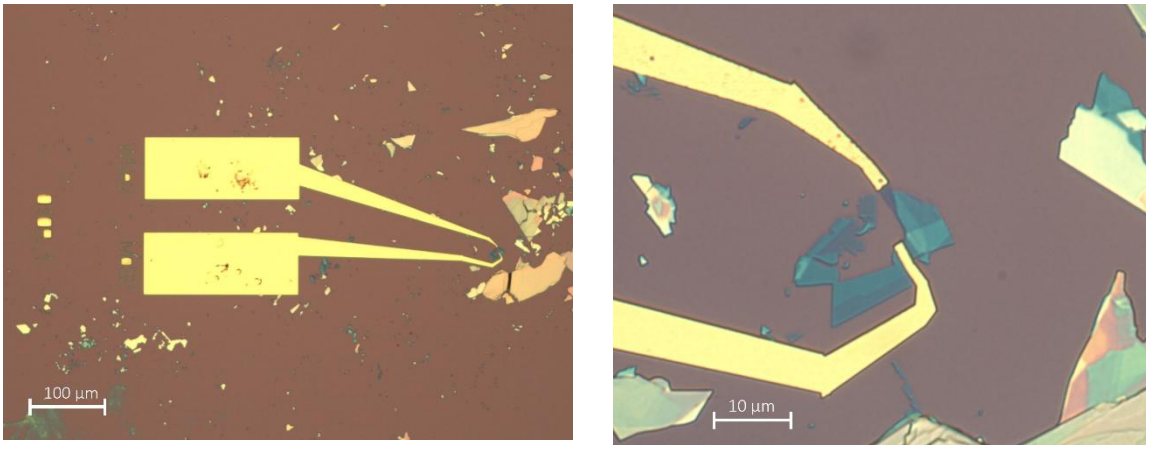

Figure 34: Contacted sample 20150109_1.

3.5. Summary of the fabrication process

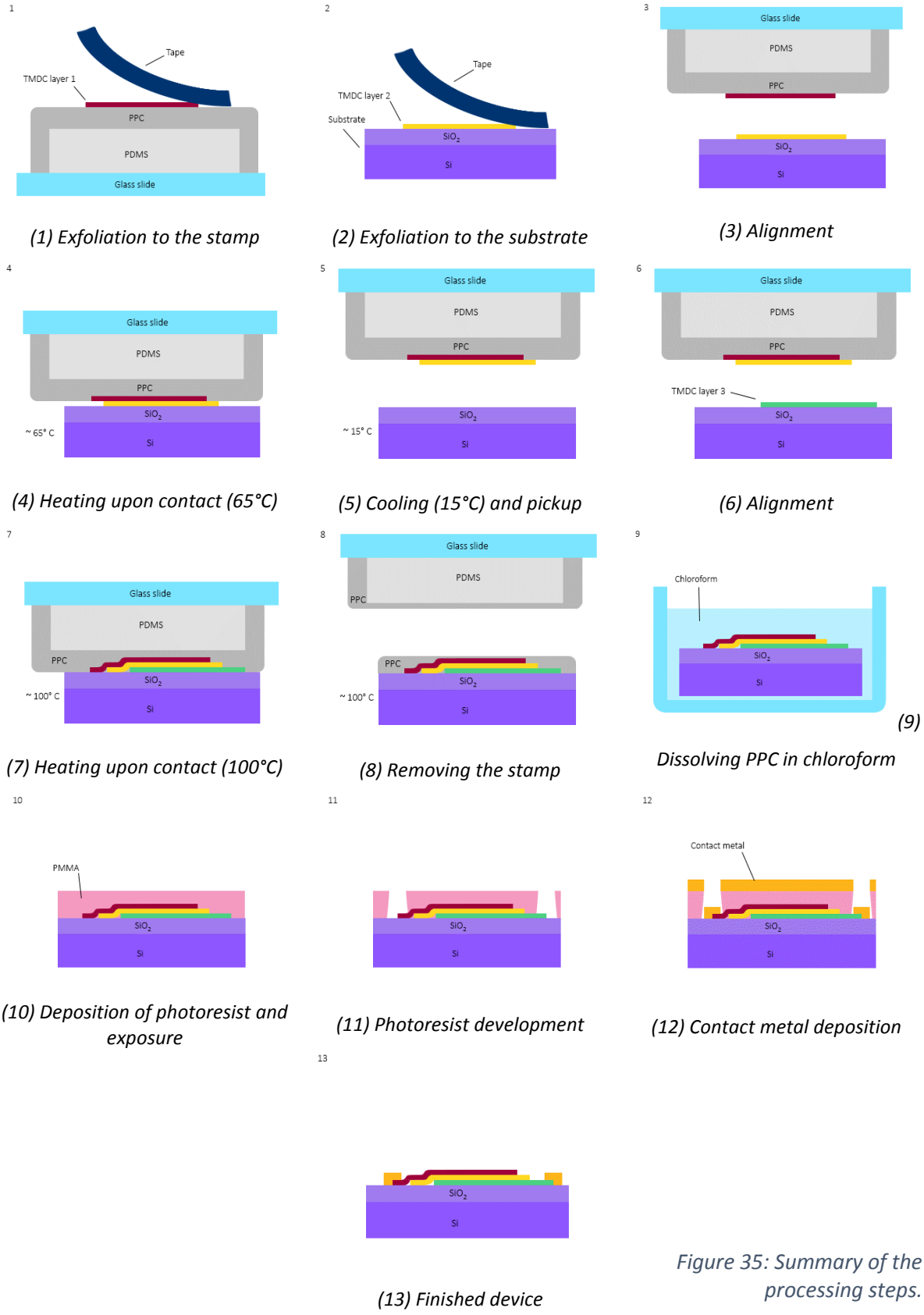

(1) Exfoliation to the stamp

(2) Exfoliation to the substrate

(3) Alignment

(4) Heating upon contact (65°C)

(5) Cooling (15°C) and pickup

(6) Alignment

(7) Heating upon contact (100°C)

(8) Removing the stamp

(9) Dissolving PPC in chloroform

(10) Deposition of photoresist and exposure

(11) Photoresist development

(12) Contact metal deposition

(13) Finished device

Figure 35: Summary of the processing steps.

4. Measurements and results

4.1. Electrical characterization

First electrical characterizations of the fabricated devices were done in a needle probe station[10] under atmospheric pressure and/or vacuum, with a semiconductor parameter analyzer[11].

The samples were placed in a vacuum chamber onto a metal sample holder which served as a backgate. The devices were contacted by Cu-Be (copper-beryllium) needles attached to micromanipulators, the voltages and currents were applied and measured by the semiconductor parameter analyzer. An optical microscope attached above the transparent cover plate of the chamber provided sight to the device for contacting, and the integrated light was utilized for illumination measurements.

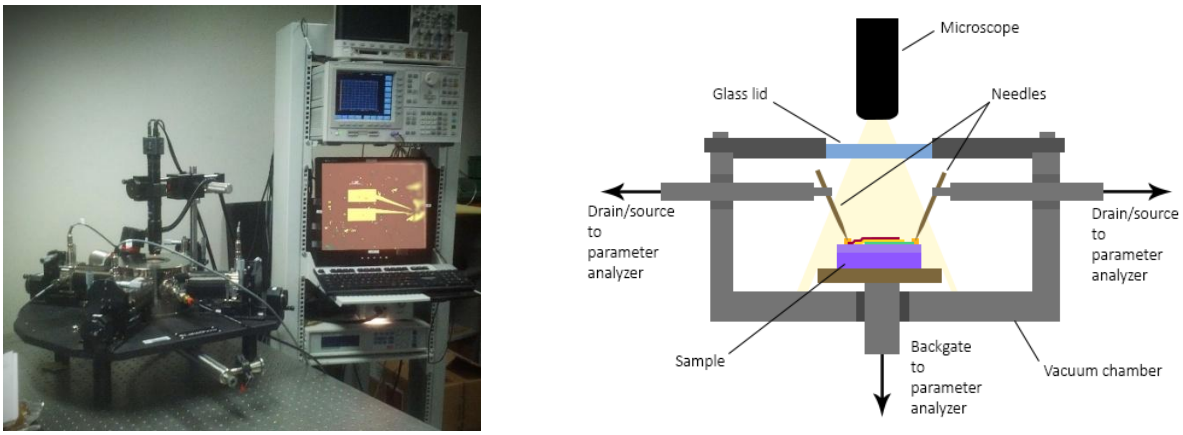

Figure 36: Picture and schematics of the probestation setup.

The devices were contacted with the drain contact applied to WSe_2 and the (grounded) source contact applied to MoS_2. The gate voltage is applied from the backside of the device between

[10] Lakeshore cryogenic probestation [87]
[11] Agilent semiconductor parameter analyzer [88]

the silicon wafer and the source contact, with isolating silicon dioxide on top of the wafer preventing shortcut.

Gate voltages were varied between +80 V and -80 V. Higher gate voltages led to a breakdown of the SiO_2 isolation and therefore were avoided. The drain-source voltage was varied in the range of +1 V and -1 V. Both drain-source current and gate-source current were recorded to prove the absence of leakage currents and their influence on drain-source current measurements.

The electric field generated by the application of a gate voltage tunes the carrier population in the energy bands of the TMDC layers. A positive gate voltage injects electrons and leads to a shift of the Fermilevel towards the conduction band, a negative gate voltage causes the opposite, as depicted in the following. Because MoS_2 is intrinsically n-doped and shows Fermilevel pinning, this effect is more pronounced in WSe_2 and WS_2 [80].

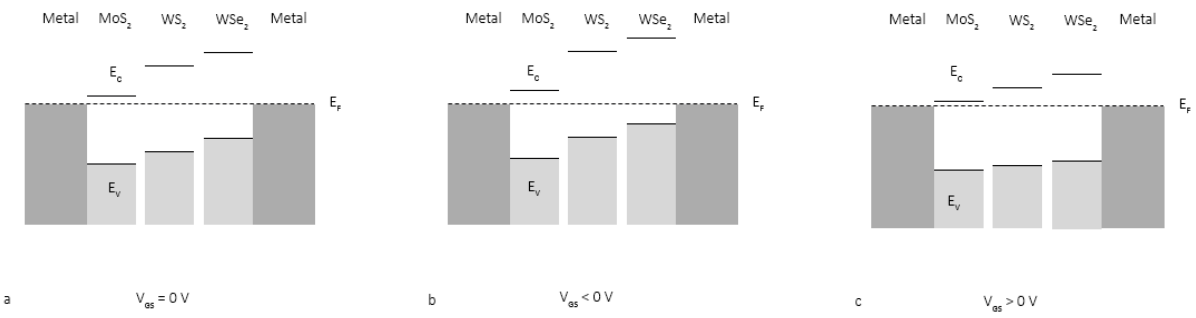

Figure 37: Expected band alignment and tuning under gate bias of the TMDC heterostructures. (a) V_{GS}=0 V (b) V_{GS}>0 V (c) V_{GS}<0 V.

When applying bias voltage to the device, two pathways can be described for the transport of charge carriers: thermionic current of thermally excited electrons via the conduction bands, and recombination (or generation) current when charge carriers recombine at the interfaces of the TMDC layers. At the interface, electron-hole pairs can also be generated by phonon or photon absorption and provide a pathway for the current. The applied bias and gate voltages influence the barrier heights and therefore determine the dominant pathway for current flow.

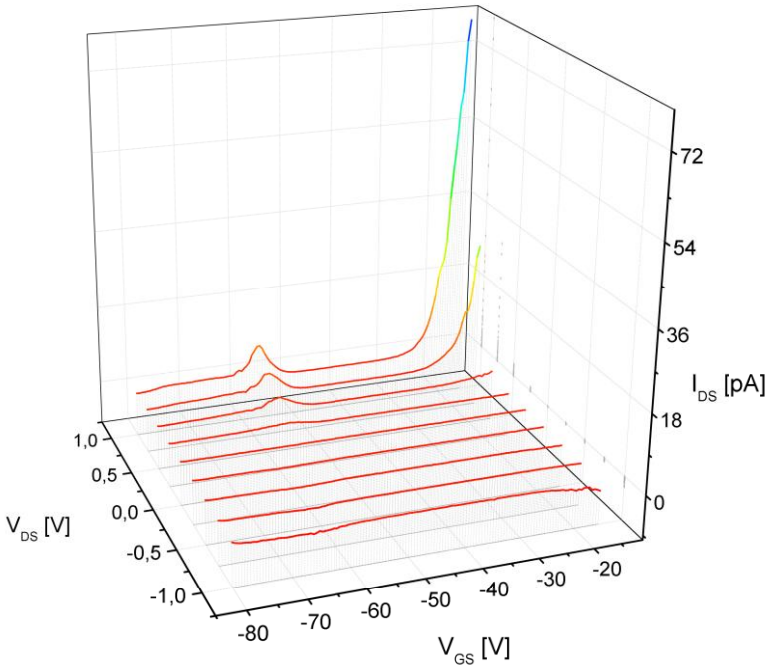

Figure 38: Drain-source current measured for various gate biases and various drain-source voltages. The p-n-type behavior is observed at gate voltages around 60 V. Currents above gate voltages of -20 V are comparably higher and are not displayed.

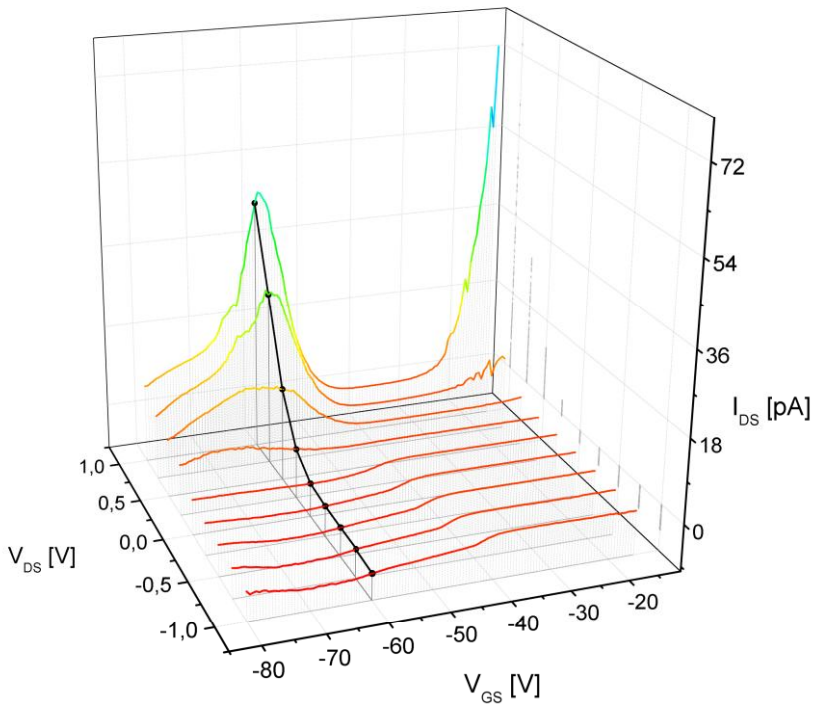

Figure 39: Equal measurement as presented in Figure 38 but repeated upon illumination. A pronounced current enhancement can be seen. The black line at V_{GS}=-60 V indicates the chosen gate voltage for further characterization.

Measurements are presented in Figure 38 and Figure 39. Above gate voltages of approximately -20 V the devices showed asymmetric but nevertheless resistive behavior, increasingly with higher positive gate voltages. This can be explained by nearly n-n type-like behavior where thermionic current mechanisms are predominant. Around approximately -60 V gate voltage the devices show typical p-n behavior, for which the recombination current mechanism can be accounted.

When applying positive gate voltage, electrons are injected into the semiconductors and thus the quasi Fermilevel is drawn close to the conduction band edge, leading to n-type behavior. Electrons can easily be injected into the conduction bands in both drain bias polarities, leading to a n-n heterojunction and showing almost ohmic resistivity. A difference in the doping as well as the connection of MoS_2 to the source contact and WSe_2 to the drain contact can be expected to come up for the asymmetry of the electrical behavior of the devices.

When negative gate voltages are applied, electrons are pushed out of the semiconductor and the quasi Fermilevel moves closer to the valence band. MoS_2 however remains n-type, whereas WSe_2 switches to p-type at a certain gate voltage. This leads to the configuration of a typical p-n junction: upon forward bias electrons are injected into MoS_2 and holes into WSe_2, which can then recombine either by tunneling through the middle layer or by thermal drift into the respective bands of the middle layer and then directly recombining at the interface. Upon reverse bias electrons and holes have to overcome a large potential height to get into the respective bands and therefore make current flow impossible.

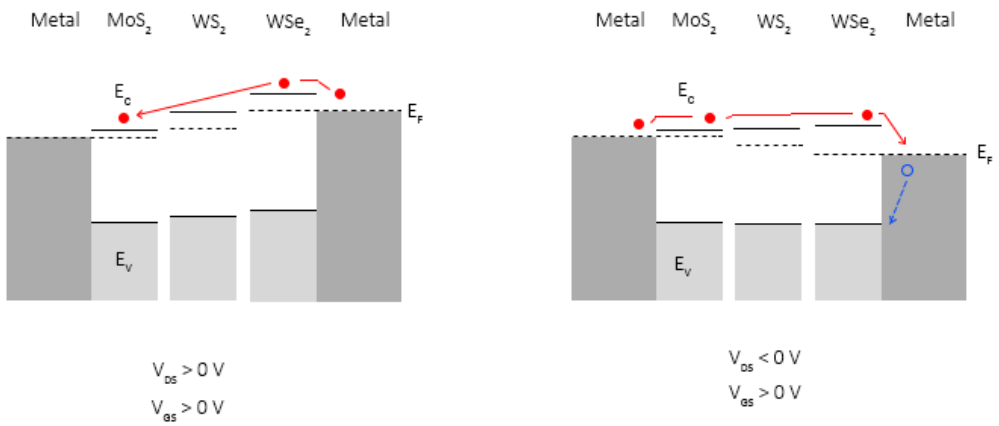

Figure 40: Carrier transport mechanisms under positive gate voltages. To the left with positive and to the right with negative drain-source bias applied. Red circles indicate electrons and blue circles indicate holes. At higher gate biases the quasi-Fermilevel is drawn even closer to the conduction band of WSe_2 leading to more pronounced n-n type behavior.

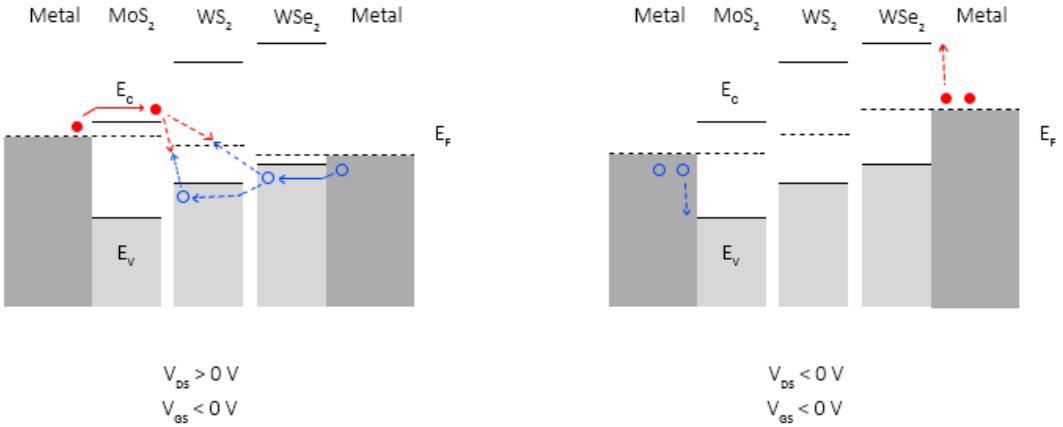

Figure 41: Carrier transport mechanisms under negative gate voltages around -60 V, depicting typical p-n type behavior. To the left with positive and to the right with negative drain-source bias applied. Positive bias enables recombination current at the TMDC interface, negative bias leads to high barriers and hinders current flow.

After first characterizations, the devices were annealed for 12 hours in high vacuum (< 10^{-6} mbar) at 100° C. This led to significant increase of the current, as shown in Figure 42, and can be attributed to the removal of water and organic residues at the interfaces of the TMDC layers.

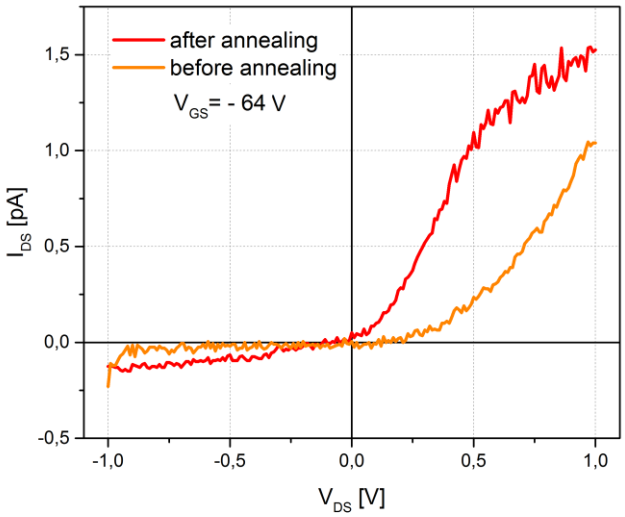

Figure 42: Current plotted over drain-source voltage before (orange) and after (red) annealing at 100° C in vacuum for 12 hours. Gate voltage was set to -64 V.

As already mentioned, electrical characterizations were also performed under illumination, showing a strong enhancement of conduction under forward bias, which can be explained by additional photon-generated charge carriers. When biased in reverse direction, a photocurrent can be observed, caused by generated charge carriers at the TMDC layer's interfaces. The typical characteristic curve of a photodiode can be observed, as shown in Figure 43. More detailed photoelectrical characterizations were performed and are presented in section 4.2.

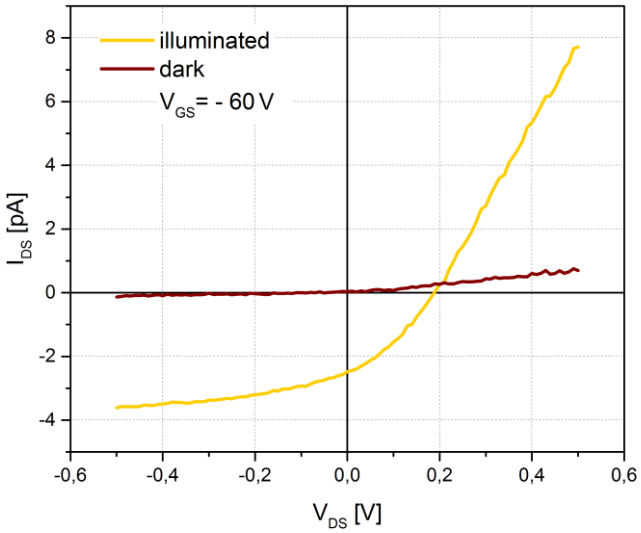

Figure 43: Drain-source IV-measurement performed in darkness (brown) and under illumination (yellow). The typical characteristic curve of a photodiode and a strong current enhancement can be seen. Gate voltage at -60 V.

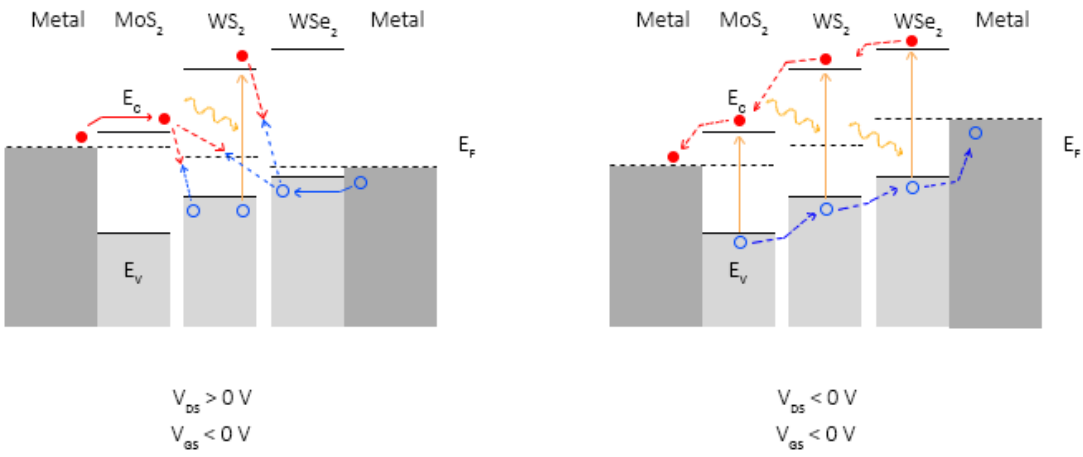

Figure 44: Illustration of the carrier transport mechanisms upon illumination. The left picture shows the forward bias case as in Figure 41, but with additional charge carriers generated by illumination enhancing the current flow. The right picture shows reverse bias, the photodiode mode. Here, only photon-generated charge carriers contribute to the current flow.

4.2. Photocurrent measurements

Photocurrent measurements were performed under atmospheric conditions in a specially designed setup. Samples were placed on a moveable sampleholder serving as a backgate contact. Drain and source were contacted by needles, both connected to a sourcemeter[12]. A solid state laser with 532 nm wavelength emitted a beam which was attenuated by neutral density filters for power control. Through coupling to an optical waveguide the beam was then coupled into an optical setup to be focused onto the sample. The exact beam position on the sample was electronically controlled by the deflection of the beam over a piezo mirror, tiltable on two axes, thus allowing raster-scanning of the probe and therefore spatially resolved measurements. The beam reflected by the sample was detected by a silicon-photodiode and measured using a lock-in amplifier[13] for noise reduction. The lock-in amplifier requires a superposition of the signal with a carrier frequency (a lock-in amplifier can be described as a narrow bandpass filter centered at the modulation frequency) and therefore necessitated modulation of the beam by a mechanical chopper. Beam splitters integrated in the optical setup additionally provided sight to the sample over an ocular for contacting and prefocusing. Lock-in amplifier and sourcemeter were connected to a computer for data recording, the piezo mirror was also controllable by a software for automated measurements.

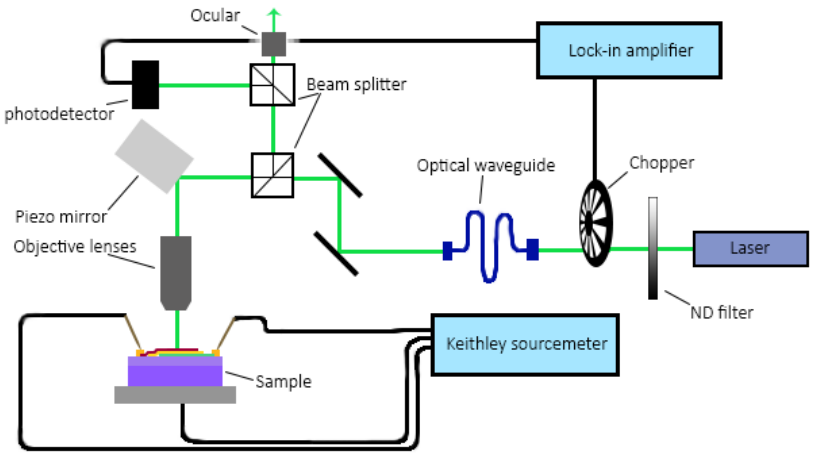

Figure 45: Schematic illustration of the photocurrent setup.

[12] Keithley dual channel system sourcemeter 2612A [89]
[13] Stanford Research Systems Lock-In Amplifier SR810 DSP [90]

Alternatively, a white light source could be coupled to the setup instead of the laser for white light photocurrent measurements and power dependent measurements. In this case spatially resolved measurements were not possible because of the larger beam diameter.

In a first step, reflection images of the sample were recorded to exactly determine the location of the device on the sample and define an adequate scanning area for further measurements. The piezo mirrors determined the exact position of the laser beam on the sample, raster scanning of the samples therefore yielded two-dimensional reflection images.

The focus of the beam was determined by a linear scan over a well defined edge (e.g. the edge of a gold contact pad) and measuring the reflectance. A steep slope in the plot of the reflection intensity indicated good focus. Furthermore, from the recorded reflection measurement the beam diameter could be calculated:

If we assume the gold pad to be an ideal reflector with a sharp edge then the reflection intensity profile can be calculated as the convolution of a function $f(x)$ and $g(x)$

$$(f * g)_{(x)} = \int_{-\infty}^{\infty} f_{(t)} g_{(x-t)} dt$$

where $f_{(x)}$ represents the intensity profile of the beam, and

$$g(x): \begin{matrix} 0 & x < 0 \\ 1 & x \geq 0 \end{matrix}$$

represents the reflectance of the scanned line, ideally being 0 at one side of the edge ($x < 0$, i.e. the substrate) and 1 at the other ($x \geq 0$, the gold contact pad). This reduces the integral to

$$(f * g)_{(x)} = \int_{0}^{\infty} f_{(t)} dt$$

Thus differentiation of the reflection signal curve should yield the intensity profile of the beam, which has been done numerically.

The measured beam profile (see Figure 46) has Gauss-like shape and could be fitted by the function

$$f_{(x)} = A \cdot e^{-\frac{(x-x_c)^2}{2\sigma^2}} + C$$

The fitted values for the constants A, x_c, σ and C are calculated to be:

$$A = -18{,}67\ (0{,}66)$$
$$C = 0{,}056\ (0{,}43)$$
$$x_c = -1{,}19 \cdot 10^{-2}\ \mu m\ (4{,}22 \cdot 10^{-3})$$
$$\sigma = 0{,}116\ \mu m\ (5{,}67 \cdot 10^{-3})$$

A can be understood as the amplitude height of the Gauss curve and is given in arbitrary units, x_c and C as shift in x and y direction, respectively. σ is the standard deviation, characterizing the width of the beam. x_c and σ are given in units of micrometers. The values in parentheses are calculated standard errors.

Thus a total beam width of about 0,7 µm can be estimated (which is about at the 3-σ-beam waist and therefore contains ~98,9% of the intensity of a two-dimensional Gauss-distributed beam).

a b

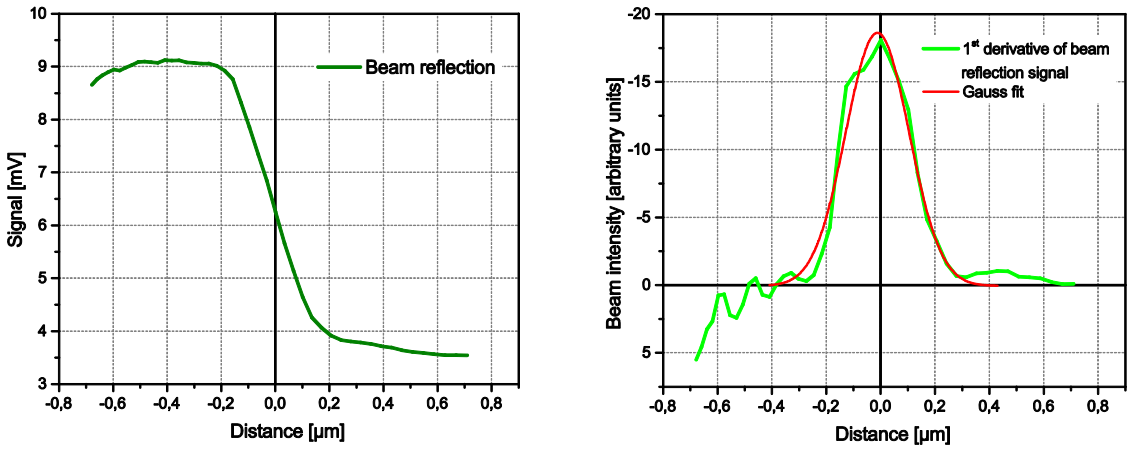

Figure 46: a: Reflection profile measured and b: calculated intensity profile. The green curve is calculated data from the reflection signal and the red curve is the fitted Gauss function. As the reflection is measured in reverse direction (from gold to the left to substrate to the right), the derivation is negative and the beam profile therefore given in negative values.

Due to this narrow beam width, highly detailled reflection images could be recorded that are fundamental for further analysis of the spatially resolved current measurements. Reflection images of the sample *20150109_1* are presented in the following.

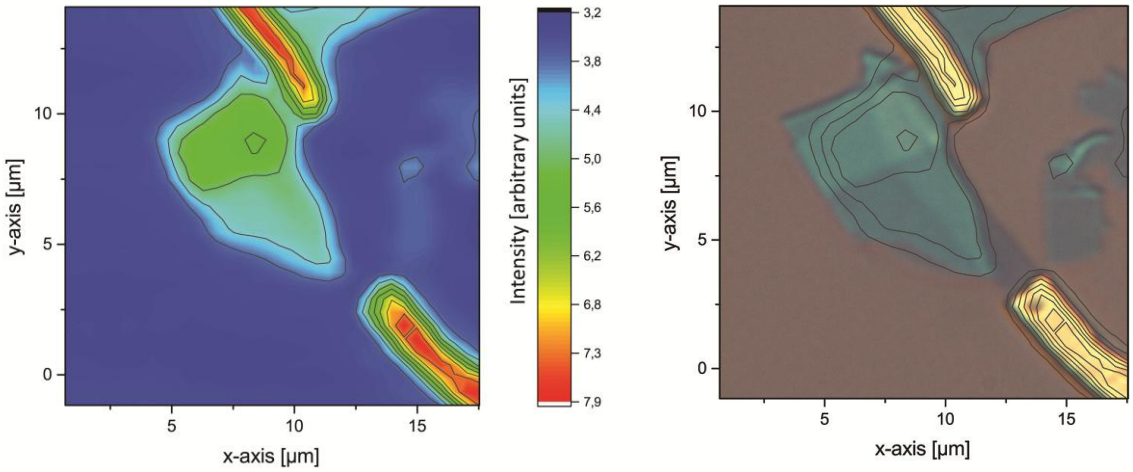

Figure 47: Reflection image of the sample 20150109_1. Device and contact fingers are recognizable. Comparison of the contour lines of the reflection image with an optical image show very good agreement.

After selection of a specific area to be scanned photocurrent measurements were performed. Again, the laser beam is raster scanned over the sample, though this time short circuit current is being measured by the keithley sourcemeter for every specific beam position, resulting in a spatially resolved map of the generation of photocurrent over the device. The gate voltage was set to -65 V to operate the device in the p-n regime. A resulting photocurrent map is presented in Figure 48.

To determine the exact location of the generated photocurrent in the device, the photocurrent maps were overlaid with the reflection contour and optical images to identify the exact location of the borders of the TMDC flakes.

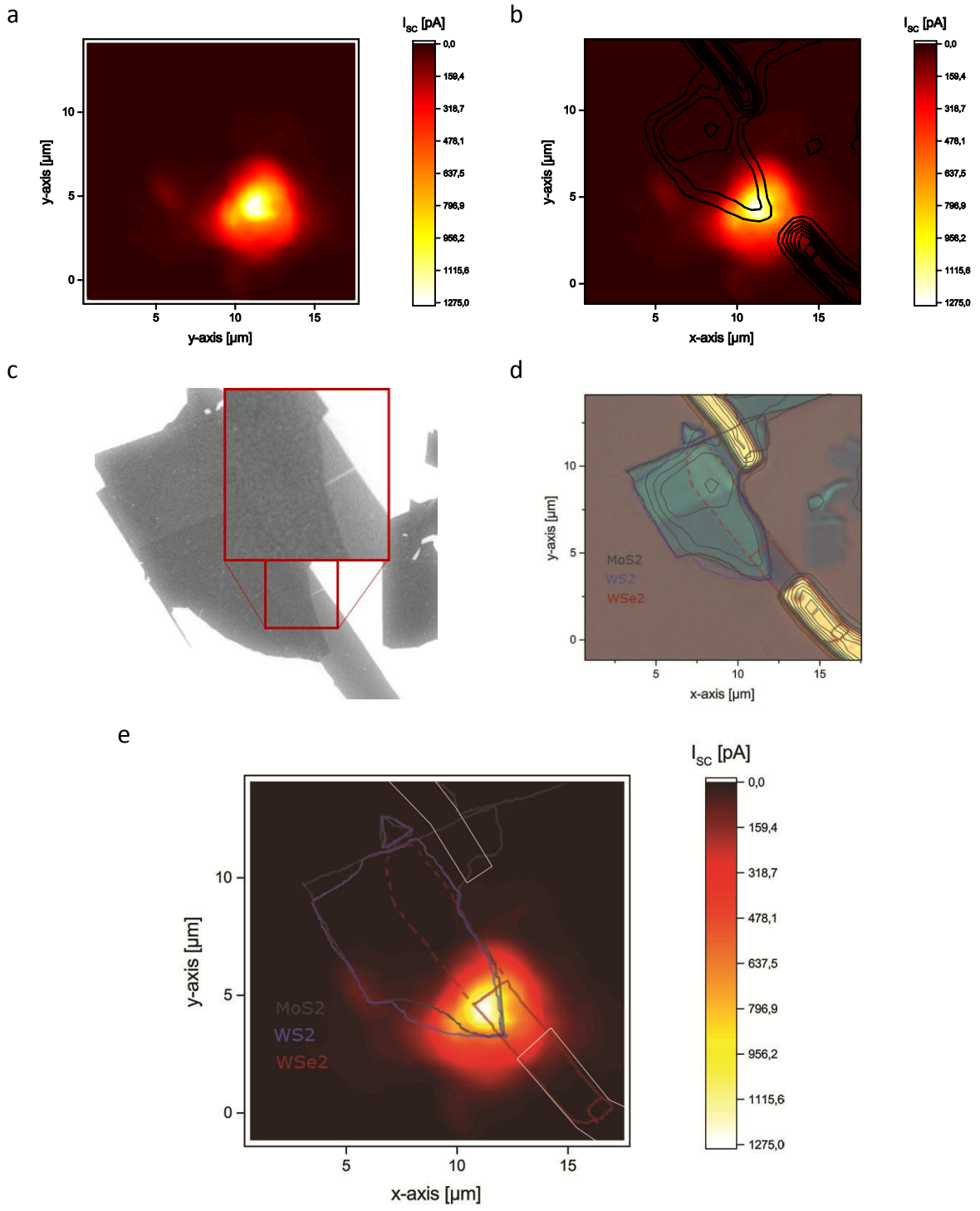

Figure 48: Photocurrent map of the device 20150109_1. The current is being generated at the overlap of all three TMDC layers. Due to a rip in the undermost WSe_2-layer the effective overlap area is reduced to the corner at the bottom of the device. (a) showing the plain photocurrent map as obtained directly from the measurement. (b) overlay of the contours of the reflection image with the photocurrent map. (c) scanning electron microscopy (SEM) image showing a tiny rip in the WSe_2 Flake, leading to a reduced effective overlap area. (d) optical image with flake edges highlighted, adjusted to the contour image. Not connected WSe_2 flake indicated by a dashed line. (e) photocurrent map with flake edges and contact fingers highlighted.

A maximum current of about 1,275 nA is measured, and as it can be seen in Figure 48, it originates from the overlap of all three TMDC layers directly connected to the contacts. A scanning electron microscopy (SEM) image of the device (Figure 48 c) shows a rip in the WSe_2-flake lying at the bottom of the stack, reducing the effective stack area connected to the contacts to the corner near the WSe_2 contact. The effective current generating area can be estimated to be about 1 µm² in size. The blurred edges of the area of photocurrent generation and the shift to areas outside the device can be accounted to the beam width and light scattering at particles around the device.

To further analyze the performance of the heterostructure when operated as a solar cell, additional measurements were performed under white light illumination with variable illumination powers. A broadband microscope light source was coupled into the setup instead of the laser and I-V measurements were performed under various illumination intensities. Again, the beam was focused over the edge of a metal contact, allowing calculations of the beam profile therefore the power distribution within the beam.

Also, a Gauss-like beam profile could be extracted and fitted with the same formula, the calculations for the fit yielded following results for the constants:

$$A = 33{,}16\ (0{,}55)$$
$$C = 0{,}82\ (0{,}34)$$
$$x_c = -0{,}83\ \mu m\ (0{,}39)$$
$$\sigma = 22{,}92\ \mu m\ (0{,}52)$$

Again, A is the amplitude, x_c and C shifts in x and y direction and σ the standard deviation. x_c and σ are given in units of micrometers, the other two in arbitrary units; values in parentheses are calculated standard errors. Hence the total beam width could be estimated to about 137 µm, thus always fully illuminating the device.

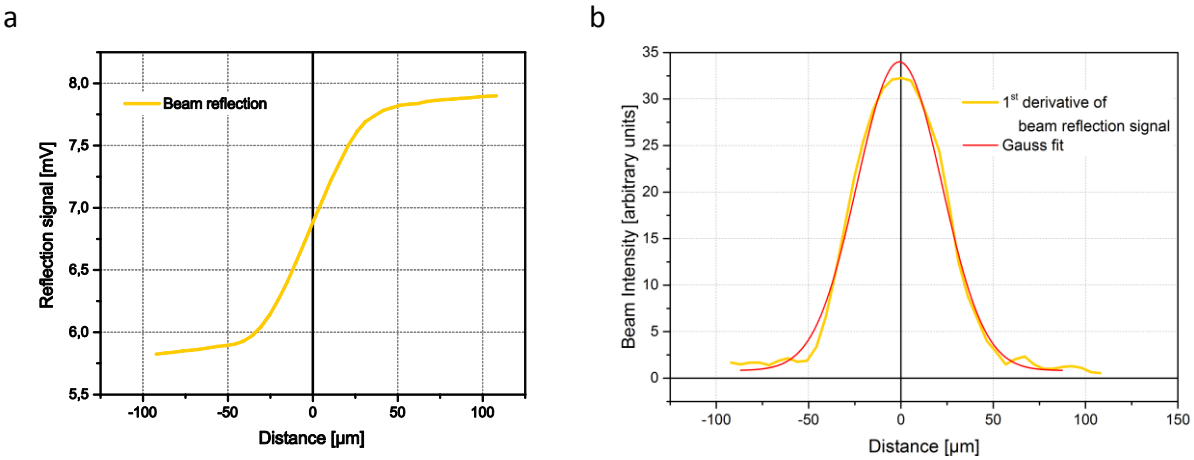

Figure 49: a: Reflection profile measured and b: calculated intensity profile to the right. The light yellow curve is calculated data from the reflection signal and the red curve is the fitted Gauss function.

Hence, not the total power of the beam is focused on the device but illuminating also the area around it. For efficiency calculations it is important to know the exact optical power reaching the device to compare it to the electrical output power. To correctly determine the effective power reaching the current generating area of the device, the beam has to be centered exactly onto device. Then the normalized two-dimensional Gauss beam profile can be integrated from the center only to the length of the extension of the device to yield the fraction of the total beam power illuminating the device itself. The two-dimensional Gauss integral (centered standard normal distribution, $x_c, y_c = 0, \sigma = 1$) is given by

$$f_{(x,y)} = A \iint_{-\infty-\infty}^{\infty\infty} e^{-\frac{x^2+y^2}{2}} dxdy$$

or when transferred to polar coordinates

$$f_{(r,\theta)} = A \iint_{0\,0}^{2\pi\,\infty} re^{-\frac{r^2}{2}} drd\theta = \int_{0}^{\infty} re^{-\frac{r^2}{2}} dr = 1$$

when normalizing with $A = \frac{1}{2\pi}$. If we now do not integrate up to ∞ but to the desired radius of our device we get the fraction of power illuminating our device. If we estimate the radius of the power generating area to be 0,5 µm, the integral yields

$$\int_0^{0,5\cdot\frac{1}{\sigma}} re^{-\frac{r^2}{2}}\,dr = 2{,}379\cdot 10^{-4}$$

In other words, about 0,24 ‰ of the total illumination power affect the device.

Measurements at eight different intensities were acquired, starting with darkness and finishing at the maximum lamp power, measured to be 443 µW optical power:

Total optical power of beam [µW]	Power on device [nW]	Intensity on device [kW/m²]
Dark	-	-
4	0,951616	1,211
63,5	15,1069	19,234
129	30,6896	39,075
238	56,6212	72,092
306	72,7986	92,69
384	91,3551	116,316
443	105,391	134,188

Table 2: Optical power emitted by the light source and the fraction impinging on the device. Another column with the intensity on the device calculated to values of kW/m² is given. Intensities correspond to about 1 to 100-fold terrestrial solar power.

The measurements are presented in the following:

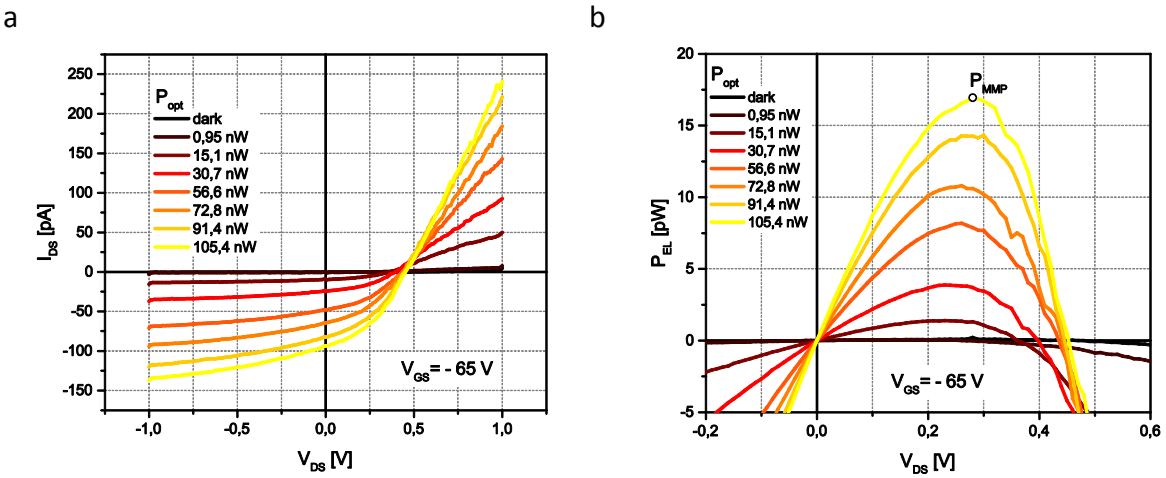

Figure 50: a: I-V curves measured under different illumination power. b: electrical power of the device plotted over gate voltage. P_{MMP} denotes the maximum power point at which the product of current and voltage is maximal. The gate voltage was set to -65 V.

a b

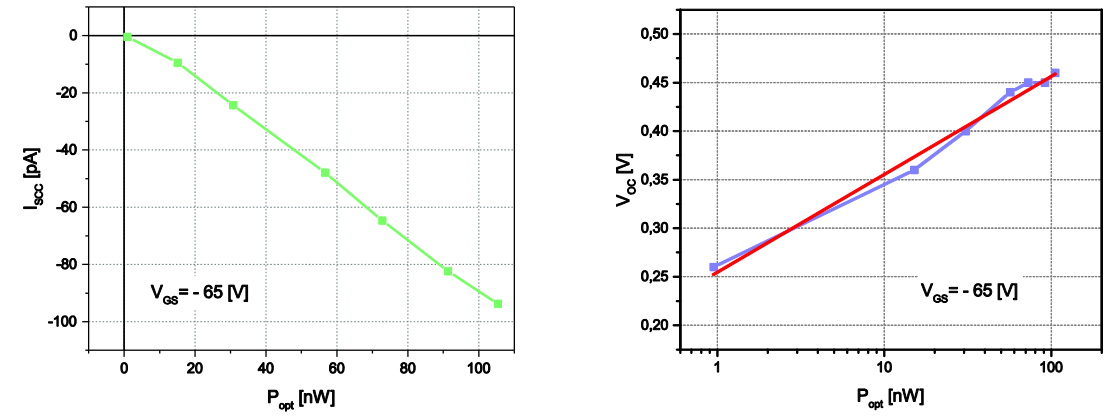

Figure 51: a: Short circuit current plotted over optical power on the device, showing linear behavior. b: Open-circuit voltage plotted over optical power on a logarithmic scale. The red line indicates a curve fit.

Short circuit current (I_{SCC}) and open circuit voltage (V_{OC}), extracted from measured curves presented in Figure 50, are plotted over optical power (P_{opt}) on the device in Figure 51. V_{OC} scales with $\log(P_{opt})$, and it can be fitted by the equation

$$V_{OC} = C + \frac{2}{\beta}\frac{k_B T}{q}\ln(P_{opt})$$

[7] which gives qualitative information about the recombination processes in the junction by the parameter β: for monomolecular (Shockley Read Hall) recombination $\beta = 1$, for bimolecular (Langevin) recombination $\beta = 2$. The fitted function is plotted in Figure 51b and indicated by a red line. $\frac{k_B T}{q} \cong 28{,}5\ mV$ at room temperature (300° K), C is fitted to 1,163, giving $\beta = 1{,}3$. This indicates that the interlayer recombination process is dominated by Shockley Read Hall recombination, pointing out a large density of trap states within the heterostructure's materials [7]. I_{SCC} however shows linear behavior and does not seem to saturate over the measured range, which goes to intensities 100-fold the terrestrial solar intensity.

Based on these values, fill factor dependency on illumination power was also calculated by $FF = P_{el,max}/(V_{OC} \cdot I_{SCC})$. The fill factor stays nearly constant over the measured range, and its value of ~0,4 is comparable to values given for amorphous silicon solar cells [81].

a b

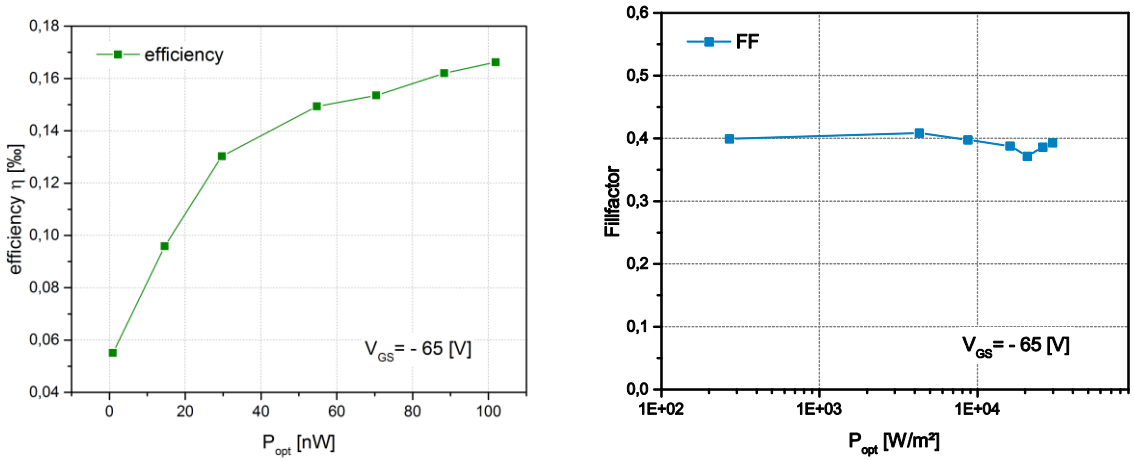

Figure 52: a: Efficiency of the device plotted over optical power on the device. The efficiency is increasing with optical power but seems to saturate at higher powers. b: fill factor plotted over optical power on the device on a logarithmic scale, it is nearly constant over all measured values.

For efficiency calculations, optical power impinging on the device has been set in relation to electrical power output of the device. The efficiency values are in the range of 0,1 - 0,2 ‰, which is about 1/10 of comparable two-dimensional cells built of only two layers. It is likely that enhanced recombination within current generation is to be accounted for the low value of our results, concomitant with the presence of more trap states induced by residue atoms between the layers, due to the doubled interface surface. But keeping in mind that the stack is only about a few nanometers thick and therefore absorbs only a fraction of the incident light, these values can be put to another perspective when comparing them to other solar cell types and different prospects on possible applications are opened: the inclusion of a resonant cavity structure or the stacking of multiple solar cell layers on top of each other could drastically enhance absorption and therefore total efficiency. On the other hand, transparent large-area coverage of windows and facades is thinkable, given that material expenses are reduced to an ultimate minimum with the usage of two-dimensional materials, high efficiency values are less substantial.

Moreover, the power densities of two dimensional materials are orders of magnitude higher than the one of conventional solar cell types (when comparing total generated power to mass

of active material) [6] and are therefore still promising candidates for future solar harvesting materials, with the potential for cheap and versatile applications due to their semi-transparency, stability and flexibility.

5. Summary and outlook

In this work, the successful fabrication of triple layer TMDC heterojunctions and their characterization is reported and their operation as solar cell is proven and analyzed.

To accomplish this, different exfoliation methods were tested and optimized to obtain optimum results by the combination of previously known methods. A reliable method for stacking of multiple TMDC layers on top of each other was needed, and was finally found within the combined usage of PDMS stamps covered by PPC foils for the successful fabrication of several TMDC heterojunctions. Electron beam lithography and electron beam physical vapor deposition were used for the processing of electrical contacts.

The devices were fabricated on top of an insulating silicon dioxide layer separating them from the highly doped silicon substrate, which served as a gate contact for following electrical characterizations. An applied electric gate field shifted the quasi-Fermi level of the TMDC layers in the heterostructures and allowed tuning of the devices' electrical properties. For gate voltages of around -60 V rectifying electrical behavior was observed, arising from a p-n like electronic configuration in the device. Upon illumination, large current enhancement could be observed, as well as a considerable photocurrent in reverse bias direction. Annealing of the devices improved their electrical properties, presumably by the removal of residues at the surface and the interfaces of the TMDC layers. This process however is limited by the thermal stability of the WSe_2 layers, which decompose above temperatures of 110°C and led to the destruction of earlier devices. Either very long annealing (over several days) at lower temperatures or finding more temperature stable alternatives to WSe_2 could anticipate possible improvement of this problem and lead to enhanced electrical and photoelectrical properties of the heterostructures.

The p-n type structure enables the operation of the devices as photodiodes and solar cells, and various measurements were performed for their characterization. Intensity dependent measurements show constant scaling of the devices properties with incident illumination power and even an improvement in efficiency. The lower efficiency compared to previously

reported solar cell devices made of two-dimensional materials [6–8] could probably be attributed to fabricational deficiencies originating from the incorporation of an additional layer, as those reported heterojunctions were built up of only two layers. The electronic configuration of three layer stacks is actually favorable because of the immediate spatial separation of generated electron-hole pairs, which should reduce the probability of recombination and had been the main motivation for this work. The inclusion of a third layer on the other hand also doubles the interface surface and therefore provides a potential for additional losses induced by residues incorporated at the interfaces leading to trap states and higher recombination rates. This circumstance is very likely to be ameliorated by finding optimized annealing conditions improving the cleanliness of the interfaces and the device itself.

Spatially resolved measurements showed the origin of the current to be exactly in the overlap area of all three flakes, proving the expected working principle of the cell. Another possibility for improvement could be given by the application of top and bottom sheets of graphene serving as contacts, making it possible to directly extract charge carriers across the whole surface, as reported in [8]. The sandwiching of the stack between layers of boron nitride could further enhance mobility as it was reported for graphene [82] and further improve total device performance.

Acronyms

AM ..... Air Mass

CdTe ..... Cadmium Telluride

CIGS ..... Copper-Indium-Gallium-Diselenide

c-Si ..... crystalline Silicon

Cu-Be ..... Copper-Beryllium

DFT ..... Density functional theory

FF ..... Fill factor

$GaInP_2$ ..... Gallium-Indium-Phosphite

GaAs ..... gallium arsenide

Ge ..... Germanium

I-V-characteristics ..... Current-Voltage characteristics

MBE ..... Molecular beam epitaxy

Mo ..... Molybdenum

MoS_2 ..... Molybdenum disulfite

$MoSe_2$ ..... Molybdenum diselenide

MX_2 ..... general chemical formular for a transition metal dichalcogenide

PDMS ..... Polydimethylsiloxane

p-n junction ..... semiconductor junction where one side acts as donor (n) and one as acceptor (p)

PMMA ..... Polymethylmethacetat

PPC ..... Polypropylcarbonate

rpm ..... rounds per minute

SEM ..... Scanning electron microscopy

Si ..... Silicon

SiO_2 ..... Silicon dioxide

TMDC ..... Transition metal dichalcogenide

W ..... Tungsten

WS_2 ..... Tungsten disulfite

WSe_2 ..... Tungsten diselenide

List of variables and constants

A	Area
α	Absorption coefficient
D_n	Diffusion constant
E	Irradiance
FF	Fillfactor
γ	Elevation angle of the sun
h	Planck's constant, $6{,}6 \cdot 10^{-34}\,Js$
I	Current
j	Emissive power density
J	Emissive power
k	Boltzmann constant, $1{,}38 \cdot 10^{-23}\,JK^{-1}$
L_n	Diffusion length
λ	Wavelength
m	Ideality factor
η	Efficiency
ν	Frequency
P	Power
P_{MMP}	Maximum Power Point
φ	Phase shift angle
q	Charge
R	Reflectance
r	Radius
σ	Stefan Boltzmann's constant, $5{,}67 \cdot 10^{-8}\ Wm^{-2}K^{-4}$
T	Temperature
τ	Lifetime (of charge carriers)
U	Voltage, general
V_{GS}, V_{DS}, V_{OC}	Gate-source/drain-source/open circuit voltage
W_{ph}, W_G	Photon energy, bandgap energy

Table of figures

References

1. K. S. Novoselov *et al.*, Electric field effect in atomically thin carbon films, *science* **306**, 666–669 (2004).

2. D. Basko, A photothermoelectric effect in graphene, *Science* **334**, 610–611 (2011).

3. M. Furchi *et al.*, Microcavity-integrated graphene photodetector, *Nano letters* **12**, 2773–2777 (2012).

4. A. K. Geim, Graphene: status and prospects, *science* **324**, 1530–1534 (2009).

5. W. Zhao, R. M. Ribeiro, G. Eda, Electronic Structure and Optical Signatures of Semiconducting Transition Metal Dichalcogenide Nanosheets, *Accounts of chemical research* **48**, 91–99 (2014).

6. M. Bernardi, M. Palummo, J. C. Grossman, Extraordinary sunlight absorption and one nanometer thick photovoltaics using two-dimensional monolayer materials, *Nano letters* **13**, 3664–3670 (2013).

7. M. M. Furchi, A. Pospischil, F. Libisch, J. Burgdörfer, T. Mueller, Photovoltaic effect in an electrically tunable van der Waals heterojunction, *Nano letters* **14**, 4785–4791 (2014).

8. C.-H. Lee *et al.*, Atomically thin p-n junctions with van der Waals heterointerfaces, *Nature nanotechnology* **9**, 676–681 (2014).

9. K. Mertens, *Photovoltaik* Hanser, Ed. (Lehrbuch zu Grundlagen, Technologie und Praxis. Fachbuchverlag, München, 2011).

10. H.-G. Wagemann, H. Eschrich, *Photovoltaik* Vieweg+ Teubner, Ed. (Springer, 2010).

11. W. Shockley, The Theory of p-n Junctions in Semiconductors and p-n Junction Transistors, *Bell System Technical Journal* **28**, 435–489 (1949).

12. D. Chapin, C. Fuller, G. Pearson, A new silicon p-n junction photocell for converting solar radiation into electrical power, *Journal of Applied Physics* **25**, 676–677 (1954).

13. W. Shockley, H. J. Queisser, Detailed balance limit of efficiency of p-n junction solar cells, *Journal of applied physics* **32**, 510–519 (1961).

14. D. Böhme, W. Dürrschmidt, M. van Mark, Renewable energy sources in figures: national and international development, *Federal Ministry for the Environment, Nature Conservation and Nuclear Safety* (2010).

15. S. Price, 2008 solar technologies market report, *Lawrence Berkeley National Laboratory* (2010).

16. Solar System Exploration: Planets: Sun: Facts & Figures (2015) (available at https://solarsystem.nasa.gov/planets/profile.cfm?Object=Sun&Display=Facts, accessed 16 Mar 2015).

17. T. Fuyuki, H. Kondo, T. Yamazaki, Y. Takahashi, Y. Uraoka, Photographic surveying of minority carrier diffusion length in polycrystalline silicon solar cells by electroluminescence, *Applied Physics Letters* **86**, 262108 (2005).

18. A. De Vos, Detailed balance limit of the efficiency of tandem solar cells, *Journal of Physics D: Applied Physics* **13**, 839 (1980).

19. S. Philipps, A. Bett, K. Horowitz, S. Kurtz, Current Status of Concentrator Photovoltaic (CPV) Technology, National Renewable Energy Laboratory (NREL), Golden, CO., (2015).

20. G. Wilson, K. Emery, (NREL), Conversion efficiencies of best research solar cells worldwide from 1976 through 2015 for various photovoltaic technologies. Efficiencies determined by certified agencies/laboratories. (2014) (available at http://commons.wikimedia.org/wiki/File:PVeff%28rev141218%29.jpg, accessed 23 Mar 2015).

21. K. V. Allamraju, K. Srikanth, Materials used for Renewable energy resources, *Advanced Materials Manufacturing & Characterization* **3**, 243-248 (2013).

22. M. A. Green, K. Emery, Y. Hishikawa, W. Warta, E. D. Dunlop, Solar cell efficiency tables (Version 45), *Progress in photovoltaics: research and applications* **23**, 1–9 (2015).

23. J. Schermer, P. Mulder, G. Bauhuis, P. Larsen, G. Oomen, E. Bongers, Thin-film GaAs epitaxial lift-off solar cells for space applications, *Progress in Photovoltaics: Research and Applications* **13**, 587–596 (2005).

24. K. Mueller, Picture: Comparison of crystalline solar cells. The ones on the left are made of multicrystalline (multi-Si), while the ones on the right are made of monocrystalline silicon (mono-Si) (2014) (available at http://commons.wikimedia.org/wiki/File:Comparison_solar_cell_poly-Si_vs_mono-Si.png#filelinks, accessed 23 Mar 2015).

25. G.-H. Lee *et al.*, Flexible and transparent MoS2 field-effect transistors on hexagonal boron nitride-graphene heterostructures, *ACS nano* **7**, 7931–7936 (2013).

26. Nobel Prize Graphene (available at http://www.nobelprize.org/nobel_prizes/physics/laureates/2010/, accessed 10 Mar 2015).

27. P. R. Wallace, The band theory of graphite, *Physical Review* **71**, 622 (1947).

28. Q. H. Wang, K. Kalantar-Zadeh, A. Kis, J. N. Coleman, M. S. Strano, Electronics and optoelectronics of two-dimensional transition metal dichalcogenides, *Nature nanotechnology* **7**, 699–712 (2012).

29. J. Wilson, A. Yoffe, The transition metal dichalcogenides discussion and interpretation of the observed optical, electrical and structural properties, *Advances in Physics* **18**, 193–335 (1969).

30. K. He, C. Poole, K. F. Mak, J. Shan, Experimental demonstration of continuous electronic structure tuning via strain in atomically thin MoS2, *Nano letters* **13**, 2931–2936 (2013).

31. W. Zhao, Z. Ghorannevis, L. Chu, M. Toh, C. Kloc, P.-H. Tan, G. Eda, Evolution of electronic structure in atomically thin sheets of WS2 and WSe2, *Acs Nano* **7**, 791–797 (2012).

32. A. Geim, I. Grigorieva, Van der Waals heterostructures, *Nature* **499**, 419–425 (2013).

33. M. Chhowalla, H. S. Shin, G. Eda, L.-J. Li, K. P. Loh, H. Zhang, The chemistry of two-dimensional layered transition metal dichalcogenide nanosheets, *Nature chemistry* **5**, 263–275 (2013).

34. G. Eda, T. Fujita, H. Yamaguchi, D. Voiry, M. Chen, M. Chhowalla, Coherent atomic and electronic heterostructures of single-layer MoS2, *ACS nano* **6**, 7311–7317 (2012).

35. K. Novoselov, D. Jiang, F. Schedin, T. Booth, V. Khotkevich, S. Morozov, A. Geim, Two-dimensional atomic crystals, *Proceedings of the National Academy of Sciences of the United States of America* **102**, 10451–10453 (2005).

36. M. Benameur, B. Radisavljevic, J. Heron, S. Sahoo, H. Berger, A. Kis, Visibility of dichalcogenide nanolayers, *Nanotechnology* **22**, 125706 (2011).

37. J. N. Coleman *et al.*, Two-dimensional nanosheets produced by liquid exfoliation of layered materials, *Science* **331**, 568–571 (2011).

38. C. Zhi, Y. Bando, C. Tang, H. Kuwahara, D. Golberg, Large-scale fabrication of boron nitride nanosheets and their utilization in polymeric composites with improved thermal and mechanical properties, *Advanced Materials* **21**, 2889–2893 (2009).

39. R. Gordon, D. Yang, E. Crozier, D. Jiang, R. Frindt, Structures of exfoliated single layers of WS 2, MoS 2, and MoSe 2 in aqueous suspension, *Physical Review B* **65**, 125407 (2002).

40. Z. Zeng *et al.*, Single-Layer Semiconducting Nanosheets: High-Yield Preparation and Device Fabrication, *Angewandte Chemie International Edition* **50**, 11093–11097 (2011).

41. H.-L. Tsai, J. Heising, J. L. Schindler, C. R. Kannewurf, M. G. Kanatzidis, Exfoliated-restacked phase of WS2, *Chemistry of materials* **9**, 879–882 (1997).

42. G. Eda, H. Yamaguchi, D. Voiry, T. Fujita, M. Chen, M. Chhowalla, Photoluminescence from chemically exfoliated MoS2, *Nano letters* **11**, 5111–5116 (2011).

43. Y.-H. Lee *et al.*, Synthesis of Large-Area MoS2 Atomic Layers with Chemical Vapor Deposition, *Advanced Materials* **24**, 2320–2325 (2012).

44. Y. Zhang *et al.*, Direct observation of the transition from indirect to direct bandgap in atomically thin epitaxial MoSe2, *Nature nanotechnology* **9**, 111–115 (2014).

45. Z. Zhu, Y. Cheng, U. Schwingenschlögl, Giant spin-orbit-induced spin splitting in two-dimensional transition-metal dichalcogenide semiconductors, *Physical Review B* **84**, 153402 (2011).

46. K. Ko'smider, J. Fernández-Rossier, Electronic properties of the MoS 2-WS 2 heterojunction, *Physical Review B* **87**, 075451 (2013).

47. A. Kumar, P. Ahluwalia, Electronic structure of transition metal dichalcogenides monolayers 1H-MX 2 (M= Mo, W; X= S, Se, Te) from ab-initio theory: new direct band gap semiconductors, *The European Physical Journal B-Condensed Matter and Complex Systems* **85**, 1–7 (2012).

48. H. R. Gutiérrez *et al.*, Extraordinary room-temperature photoluminescence in triangular WS2 monolayers, *Nano letters* **13**, 3447–3454 (2012).

49. J. S. Ross *et al.*, Electrically tunable excitonic light-emitting diodes based on monolayer WSe2 pn junctions, *Nature nanotechnology* **9**, 268–272 (2014).

50. A. Splendiani *et al.*, Emerging photoluminescence in monolayer MoS2, *Nano letters* **10**, 1271–1275 (2010).

51. L. Kou, T. Frauenheim, C. Chen, Nanoscale Multilayer Transition-Metal Dichalcogenide Heterostructures: Band Gap Modulation by Interfacial Strain and Spontaneous Polarization, *The Journal of Physical Chemistry Letters* **4**, 1730–1736 (2013).

52. A. Kuc, N. Zibouche, T. Heine, Influence of quantum confinement on the electronic structure of the transition metal sulfide T S 2, *Physical Review B* **83**, 245213 (2011).

53. J. Kang, S. Tongay, J. Zhou, J. Li, J. Wu, Band offsets and heterostructures of two-dimensional semiconductors, *Applied Physics Letters* **102**, 012111 (2013).

54. K. F. Mak, C. Lee, J. Hone, J. Shan, T. F. Heinz, Atomically thin MoS 2: a new direct-gap semiconductor, *Physical Review Letters* **105**, 136805 (2010).

55. H. Fang *et al.*, Strong interlayer coupling in van der Waals heterostructures built from single-layer chalcogenides, *Proceedings of the National Academy of Sciences* **111**, 6198–6202 (2014).

56. A. Hanbicki, M. Currie, G. Kioseoglou, A. Friedman, B. Jonker, Measurement of high exciton binding energy in the monolayer transition-metal dichalcogenides WS 2 and WSe 2, *Solid State Communications* **203**, 16–20 (2015).

57. P. Johari, V. B. Shenoy, Tuning the electronic properties of semiconducting transition metal dichalcogenides by applying mechanical strains, *ACS nano* **6**, 5449–5456 (2012).

58. B. Radisavljevic, A. Radenovic, J. Brivio, V. Giacometti, A. Kis, Single-layer MoS2 transistors, *Nature nanotechnology* **6**, 147–150 (2011).

59. G.-H. Lee *et al.*, Heterostructures based on inorganic and organic van der Waals systems, *APL Materials* **2**, 092511 (2014).

60. N. Lu *et al.*, MoS 2/MX 2 heterobilayers: bandgap engineering via tensile strain or external electrical field, *Nanoscale* **6**, 2879–2886 (2014).

61. J. Kang, J. Li, S.-S. Li, J.-B. Xia, L.-W. Wang, Electronic structural Moiré pattern effects on MoS2/MoSe2 2D heterostructures, *Nano letters* **13**, 5485–5490 (2013).

62. www.2spi.com, SPI Supplies® Brand Moly Disulfide (MoS2) (available at http://www.2spi.com/catalog/molybdenum.shtml, accessed 24 Mar 2015).

63. HQGraphene.com, MoS2, MoSe2, MoTe2 large size single crystals, HQGraphene.com (available at http://hqgraphene.com/PeriodicTableElements/Mo.php, accessed 24 Mar 2015).

64. nanoscience.com, WSe2 nanosurf (available at http://store.nanoscience.com/store/pc/viewPrd.asp?idproduct=155#details, accessed 24 Mar 2015).

65. www.2dsemiconductors.com, 2DSemiconductors.com: Tungsten Disulfide (WS2) (available at http://www.2dsemiconductors.com/Tungsten-disulfide-WS2-p/blkws2.htm, accessed 24 Mar 2015).

66. Si-Mat Silicon Materials (available at http://si-mat.com/de/impressum.html, accessed 24 Mar 2015).

67. M. J. Allen *et al.*, Soft transfer printing of chemically converted graphene, *Advanced Materials* **21**, 2098–2102 (2009).

68. X. Feng, M. A. Meitl, A. M. Bowen, Y. Huang, R. G. Nuzzo, J. A. Rogers, Competing fracture in kinetically controlled transfer printing, *Langmuir* **23**, 12555–12560 (2007).

69. Clariant GmbH Rheingaustrasse 190 D-65203 Wiesbaden, Product Data Sheet AZ 5214 Photoresist.

70. B. A. Langowski, K. E. Uhrich, Oxygen plasma-treatment effects on Si transfer, *Langmuir* **21**, 6366–6372 (2005).

71. C. Thibault, C. Séverac, A.-F. Mingotaud, C. Vieu, M. Mauzac, Poly (dimethylsiloxane) contamination in microcontact printing and its influence on patterning oligonucleotides, *Langmuir* **23**, 10706–10714 (2007).

72. A. Pospischil, Electrical transport in atommically thin MoS2 layers, masterthesis, TU Vienna (2012).

73. A. Castellanos-Gomez, M. Buscema, R. Molenaar, V. Singh, L. Janssen, H. S. van der Zant, G. A. Steele, Deterministic transfer of two-dimensional materials by all-dry viscoelastic stamping, *2D Materials* **1**, 011002 (2014).

74. L. Wang *et al.*, One-dimensional electrical contact to a two-dimensional material, *Science* **342**, 614–617 (2013).

75. Allresist GMBH, Positive PMMA E-Beam Resists AR-P 630 – 670 series product information (available at http://www.allresist.com/wp-content/uploads/sites/2/2014/02/allresist_produktinfos_ar-p630-690_englisch.pdf, accessed 25 Mar 2015).

76. A. A. Tseng, K. Chen, C. D. Chen, K. J. Ma, Electron beam lithography in nanoscale fabrication: recent development, *Electronics Packaging Manufacturing, IEEE Transactions on* **26**, 141–149 (2003).

77. K. Cai, M. Müller, J. Bossert, A. Rechtenbach, K. D. Jandt, Surface structure and composition of flat titanium thin films as a function of film thickness and evaporation rate, *Applied Surface Science* **250**, 252–267 (2005).

78. L. Gavioli, K. R. Kimberlin, M. C. Tringides, J. F. Wendelken, Z. Zhang, Novel growth of Ag islands on Si (111): Plateaus with a singular height, *Physical review letters* **82**, 129 (1999).

79. K. S. Yoo, I. W. Sorensen, W. S. Glaunsinger, Adhesion, surface morphology, and gas sensing characteristics of thin-gold-film chemical sensors, *Journal of Vacuum Science & Technology A* **12**, 192–198 (1994).

80. C. Gong, L. Colombo, R. M. Wallace, K. Cho, The unusual mechanism of partial Fermi level pinning at metal-MoS2 interfaces, *Nano letters* **14**, 1714–1720 (2014).

81. A. Alkaya, R. Kaplan, H. Canbolat, S. Hegedus, A comparison of fill factor and recombination losses in amorphous silicon solar cells on ZnO and SnO 2, *Renewable Energy* **34**, 1595–1599 (2009).

82. C. Dean *et al.*, Boron nitride substrates for high-quality graphene electronics, *Nature nanotechnology* **5**, 722–726 (2010).

83. SYLGARD® 184 SILICONE ELASTOMER KIT (available at http://www.dowcorning.com/applications/search/products/details.aspx?prod=01064291, accessed 24 Mar 2015).

84. Hettich Zentrifugen, EBA 20 (available at http://www.hettich.ch/de/produkte/hettich-zentrifugen/klein-zentrifugen/eba-20, accessed 24 Mar 2015).

85. Photoresist AZ 5214, Microchemicals (available at http://www.microchemicals.com/products/photoresists/az_5214e.html, accessed 24 Mar 2015).

86. Raith GmbH, Raith eline (available at https://www.raith.com/products/eline-plus.html, accessed 24 Mar 2015).

87. Lake Shore Cryotronics Inc., Lakeshore Cryogenic Probe Station PS-100 (available at http://www.lakeshore.com/products/Cryogenic-Probe-Stations/Model-PS-100-Tabletop-Cryogenic-Probe-Station/Pages/Overview.aspx, accessed 27 Mar 2015).

88. Keysight Technologies GmbH, 4155C Semiconductor Parameter Analyzer (available at http://www.keysight.com/en/pd-153734-pn-4155C/semiconductor-parameter-analyzer?cc=AT&lc=ger, accessed 27 Mar 2015).

89. Keithley Instruments Inc., Keithley Model 2612A Dual-channel System SourceMeter Instrument (200V, 10A Pulse) (available at http://www.keithley.com/products/dcac/currentvoltage/gpmp/?mn=2612A, accessed 27 Mar 2015).

90. Stanford Research Systems Inc., Stanford Research Systems Lock-In Amplifier SR810 DSP (available at http://www.thinksrs.com/products/SR810830.htm, accessed 27 Mar 2015).